Redox Biology 65 (2023) 102833

Contents lists available at ScienceDirect

Redox Biology

journal homepage: www.elsevier.com/locate/redox

Loss of PERK function promotes ferroptosis by downregulating SLC7A11 (System Xc⁻) in colorectal cancer

Krishan Kumar Saini [a,b], Priyank Chaturvedi [a], Abhipsa Sinha [a], Manish Pratap Singh [a], Muqtada Ali Khan [a], Ayushi Verma [a], Mushtaq Ahmad Nengroo [a], Saumya Ranjan Satrusal [a,b], Sanjeev Meena [a], Akhilesh Singh [a], Sameer Srivastava [c], Jayanta Sarkar [a,b], Dipak Datta [a,b,*]

[a] Division of Cancer Biology, CSIR-Central Drug Research Institute (CDRI), Lucknow, 226031, India
[b] Academy of Scientific and Innovative Research, Ghaziabad, Uttar Pradesh, 201002, India
[c] Department of Biotechnology, Motilal Nehru National Institute of Technology Allahabad, Prayagraj, 211004, India

ARTICLE INFO

Keywords:
ER stress
UPR
PERK
SLC7A11
Ferroptosis
Cancer

ABSTRACT

Ferroptosis, a genetically and biochemically distinct form of programmed cell death, is characterised by an iron-dependent accumulation of lipid peroxides. Therapy-resistant tumor cells display vulnerability toward ferroptosis. Endoplasmic Reticulum (ER) stress and Unfolded Protein Response (UPR) play a critical role in cancer cells to become therapy resistant. Tweaking the balance of UPR to make cancer cells susceptible to ferroptotic cell death could be an attractive therapeutic strategy. To decipher the emerging contribution of ER stress in the ferroptotic process, we observe that ferroptosis inducer RSL3 promotes UPR (PERK, ATF6, and IRE1α), along with overexpression of cystine-glutamate transporter SLC7A11 (System Xc⁻). Exploring the role of a particular UPR arm in modulating SLC7A11 expression and subsequent ferroptosis, we notice that PERK is selectively critical in inducing ferroptosis in colorectal carcinoma. PERK inhibition reduces ATF4 expression and recruitment to the promoter of *SLC7A11* and results in its downregulation. Loss of PERK function not only primes cancer cells for increased lipid peroxidation but also limits in vivo colorectal tumor growth, demonstrating active signs of ferroptotic cell death *in situ*. Further, by performing TCGA data mining and using colorectal cancer patient samples, we demonstrate that the expression of *PERK* and *SLC7A11* is positively correlated. Overall, our experimental data indicate that PERK is a negative regulator of ferroptosis and loss of PERK function sensitizes colorectal cancer cells to ferroptosis. Therefore, small molecule PERK inhibitors hold huge promise as novel therapeutics and their potential can be harnessed against the apoptosis-resistant condition.

1. Introduction

Cancer is a leading cause of death worldwide; in 2020, there were 19.3 million new cases of all types of cancer in which more than half of the patients died. Colorectal cancer is the third most commonly diagnosed cancer (10.0%) and the second leading cause of death (9.4%) worldwide in both males and females [1]. Therapy resistance is the key to tumor relapse and subsequent tumor-associated mortality. Evasion of apoptosis is one of the important hallmarks of cancer cells and mechanisms behind the same have enormous therapeutic potential in the context of current cancer research [2]. Recently, we have shown how intracellular CXCR4 protein and epigenetic modulator EZH2 promote therapy resistance, CSC properties and metastasis in colorectal and breast cancer [3–5]. Recent reports also suggest that these resistant cancer cells are vulnerable to iron-mediated cell death or 'Ferroptosis' [6,7].

As originally discovered by the Stockwell group, ferroptosis is morphologically, biochemically and genetically distinct from apoptosis, necroptosis, and autophagy and depends on intracellular iron [8,9]. Selenoprotein Glutathione peroxidase 4 (GPx4), cystine/glutamate antiporter (System Xc⁻) and enzyme Acyl-CoA synthetase long-chain family member 4 (ACSL4) are known to be the key modulators of ferroptotic process [10–12]. GPx4 is the critical enzyme that can reduce lipid hydroperoxides within biological membranes; hence ferroptosis can be induced by the treatment of small molecule GPx4 inhibitor RSL3 (Ras Selective Lethal) treatment [13,14]. SLC7A11 or System Xc⁻ is a multi-pass transmembrane protein that facilitates the export of intracellular glutamate and import of extracellular cystine in a 1:1 ratio [15].

* Corresponding author. Division of Cancer Biology, CSIR-CDRI, B.S. 10/1, Sector 10, Jankipuram Extension, Sitapur Road, Lucknow, 226031, India.
E-mail address: dipak.datta@cdri.res.in (D. Datta).

https://doi.org/10.1016/j.redox.2023.102833
Received 28 June 2023; Received in revised form 26 July 2023; Accepted 27 July 2023
Available online 28 July 2023

Following cellular absorption, cystine (dimer) is reduced to form cysteine (monomer), which serves as the rate-limiting precursor for glutathione (GSH) synthesis [16]. GPx4 mediates the conversion of toxic lipid peroxides to nontoxic lipid alcohols in the presence of GSH [17]. Inhibition of SLC7A11 results in GSH depletion, which in turn decreases GPx4 activity, leading to the damage of cellular/subcellular membranes caused by the accumulation of iron-dependent lipid peroxides or ferroptosis [18,19]. On the other hand, ACSL4 modulates ferroptosis sensitivity by shaping the cellular lipid composition of the cell [20].

Though therapy-resistant cells have vulnerability to ferroptotic cell death, these cells are proficient in handling therapeutic insults by adapting to cellular stress caused by Unfolded Protein Response (UPR) [21]. UPR is initiated by three transmembrane proteins PERK (Protein kinase RNA-like endoplasmic reticulum kinase), ATF6 (activating transcription factor 6), IRE1α (inositol-requiring enzyme 1α), which are commonly known as three arms of UPR [22,23]. These three proteins are responsible for maintaining cell survival and homeostasis by regulating protein folding in response to UPR [24]. These proteins have an ER-luminal domain believed to sense the protein misfolding; alteration in this domain in response to stress also changes the oligomerization state of these UPR proteins. PERK and IRE1α only need the oligomerization of the luminal domain to be activated; an ER chaperone Bip/GRP78 binding keeps these two proteins inactive by maintaining these proteins in ER membrane in unstressed cell conditions [25,26]. PERK has a single kinase domain that limits eIF2α activity by phosphorylating it, resulting in global translation attenuation, whereas ATF4 translation is selectively upregulated when active eIF2α is limiting [27]. IRE1α possesses kinase and RNase activity; when activated, IRE1α cleaves *XBP1*, and *XBP1* then activates transcription of many ER-related genes that regulate protein folding in the ER [28,29]. ATF6 is translocated to the Golgi lumen and cleaved by site-1 protease (S1P) and Site-2 protease (S2P) to produce ATF6 (N). ATF6 (N) and XBP1 promote protein transcription, which increases ER size and protein folding capacity [30,31]. These transcriptional processes work in concert as homeostatic feedback loops to reduce ER stress. If the amount of misfolded protein is declined, UPR signaling is decreased and the cell survives.

The influence of UPR in regulating tumor cell apoptosis and autophagic cell death is vastly studied in the literature [32,33]. Ferroptosis-induced ER stress has been documented previously [34], however, very little is known regarding the role of UPR in modulating ferroptosis. Here, we reveal that ferroptosis inducer RSL3 promotes an enormous amount of ER stress in colorectal cancer cells. In the course of dissecting the impact of three independent UPR arms in modulating RSL3 induced ferroptosis, we observe that among all three arms of UPR, PERK selectively prevents ferroptotic tumor cell death. Further analysis suggests that PERK activation and downstream signaling protects tumor cells from ferroptosis through SLC7A11 upregulation. Similarly, loss of PERK function results in reduced colorectal tumor growth in vivo with increased ferroptosis. Finally, TCGA data mining and expression analysis of colorectal cancer patient-derived tumors with their matched normal counterpart display a positive correlation between *PERK* and *SLC7A11* expression signifying the clinical relevance of our finding.

2. Results

2.1. PERK arm of UPR positively regulates SLC7A11 (System Xc⁻) expression in colorectal cancer cells

The relationship between apoptosis/autophagic cell death and UPR or ER stress is well established. However, the contribution of UPR in modulating ferroptotic cell death in colorectal cancer remains elusive. To investigate the above relationship, first, we tested the impact of ferroptosis inducer (RSL3) on three different arms of UPR (PERK, ATF6 and IRE1α) in different colorectal cancer cells HT29, SW620, DLD1, and HCT116. As shown in Fig. 1A–D, classical ferroptosis inducer RSL3 promotes the expression of three arms of UPR in all four colorectal cancer cells. In all the cases, RSL3 not only increases PERK protein expression but also promotes PERK phosphorylation as indicated by the upward shift of the PERK band as PERK has multiple phosphorylation sites. As expected, we also find similar upregulation of downstream effector proteins of UPR, such as ATF4 and Bip/GRP78 following RSL3 treatment (Supplementary Fig. 1) in CRC cells. Further, we evaluated its effect on the expression of ferroptosis signature genes, such as *GPx4, ACSL4*, and *SLC7A11*. As observed in Fig. 1E, being a GPx4 inhibitor, RSL3 treatment inhibits GPx4 expression as expected, whereas the expression of SLC7A11 is markedly upregulated in HT29 cells, having no impact on ACSL4 expression. Similar results are obtained in other CRC cells (Supplementary Fig. 2). Further, we sought to determine the role of three different UPR arms in the expression of ferroptosis signature genes *GPx4, ACSL4*, and *SLC7A11* in HT29 colorectal cancer cells. In Fig. 1F–H, we observe individual knockdowns of each UPR arm like PERK, ATF6 and IRE1α in HT29 cells, resulting in non-noticeable changes in protein expression of ferroptotic genes except PERK knockdown markedly reduces the expression of SLC7A11 protein as compared to control. Since RSL3 was shown to upregulate SLC7A11 expression at basal conditions, we evaluated the effect of RSL3 on PERK genetic and pharmacological silencing in CRC cells. PERK knockdown prevented RSL3 induced SLC7A11 overexpression in both HT29 (Fig. 1I) and SW620 (Supplementary Fig. 3) cells as compared to their respective controls. Similarly, loss of PERK function (kinase activity inhibition) by PERK inhibitor (GSK2656157) treatment results in dramatic reduction of SLC7A11 expression in HT29 (Fig. 1J) and other CRC cells (Supplementary Fig. 4). We further treated HT29 cells either with RSL3 alone or in combination with PERK kinase inhibitor GSK2656157 and found that PERK inhibitor also mitigates RSL3 induced SLC7A11 expression (Fig. 1K). Therefore, either the loss of PERK protein or functional loss of PERK kinase activity through PERK inhibitor dampens SLC7A11 expression at the basal conditions and abrogates RSL3-mediated SLC7A11 induction. Additionally, we cultured EV and PERK knockdown HT29 and SW620 cells for 72 h in cystine^{+} and cystine^{-} conditions and observed that SLC7A11 expression is upregulated in cystine^{-} conditions as compared to cystine^{+} control. The above phenomenon is significantly abolished in PERK knockdown in HT29 and SW620 cells (Fig. 1L-M, left panel), suggesting that PERK is indispensable for SLC7A11 upregulation in cystine-starved conditions. Further, the pictorial representation (Supplementary Fig. 5, upper panel) and densitometric quantification (Fig. 1L-M right panel), show a significant reduction in cell number (area covered) in PERK knockdown condition compared to the respective control when cells are cultured without cystine. As shown in Fig. 1N-O and Supplementary Fig. 5, bottom panel, we also cultured PERK inhibitor-treated HT29 and SW620 cells in cystine^{+} and cystine^{-} conditions for 72 h and observed that PERK functional inhibition reduces SLC7A11 expression in both the culture conditions and inhibits cell viability in cystine^{-} condition. Above findings suggest that either the genetic loss of PERK protein or functional loss of PERK kinase activity through PERK inhibitor treatment reduces cell viability in cystine^{-} conditions and dampens SLC7A11 expression not only at basal condition but also abrogates RSL3 mediated SLC7A11 induction.

2.2. PERK loss of function sensitizes colorectal cancer cells to ferroptosis

SLC7A11 (System Xc⁻) is a vital membrane transporter that imports cystine into the cytosol in exchange for glutamate, while glutathione synthetase (GS) and γ-glutamylcysteine synthetase (GCS) synthesize the antioxidant and GPx4 substrate glutathione. Our prior findings show that loss of PERK reduces System Xc⁻ expression, implying that this down-regulation might play a role in ferroptosis regulation. So, we treated different UPR arm knockdown HT29 cells with RSL3 and observed that PERK knockdown cells are more selectively sensitive to RSL3 mediated cell death than vehicle control, ATF6 KD, or IRE1α KD cells (Fig. 2A and Supplementary Fig. 6, top panel). PERK knockdown in SW620 cells produces similar results (Fig. 2B and Supplementary Fig. 6,

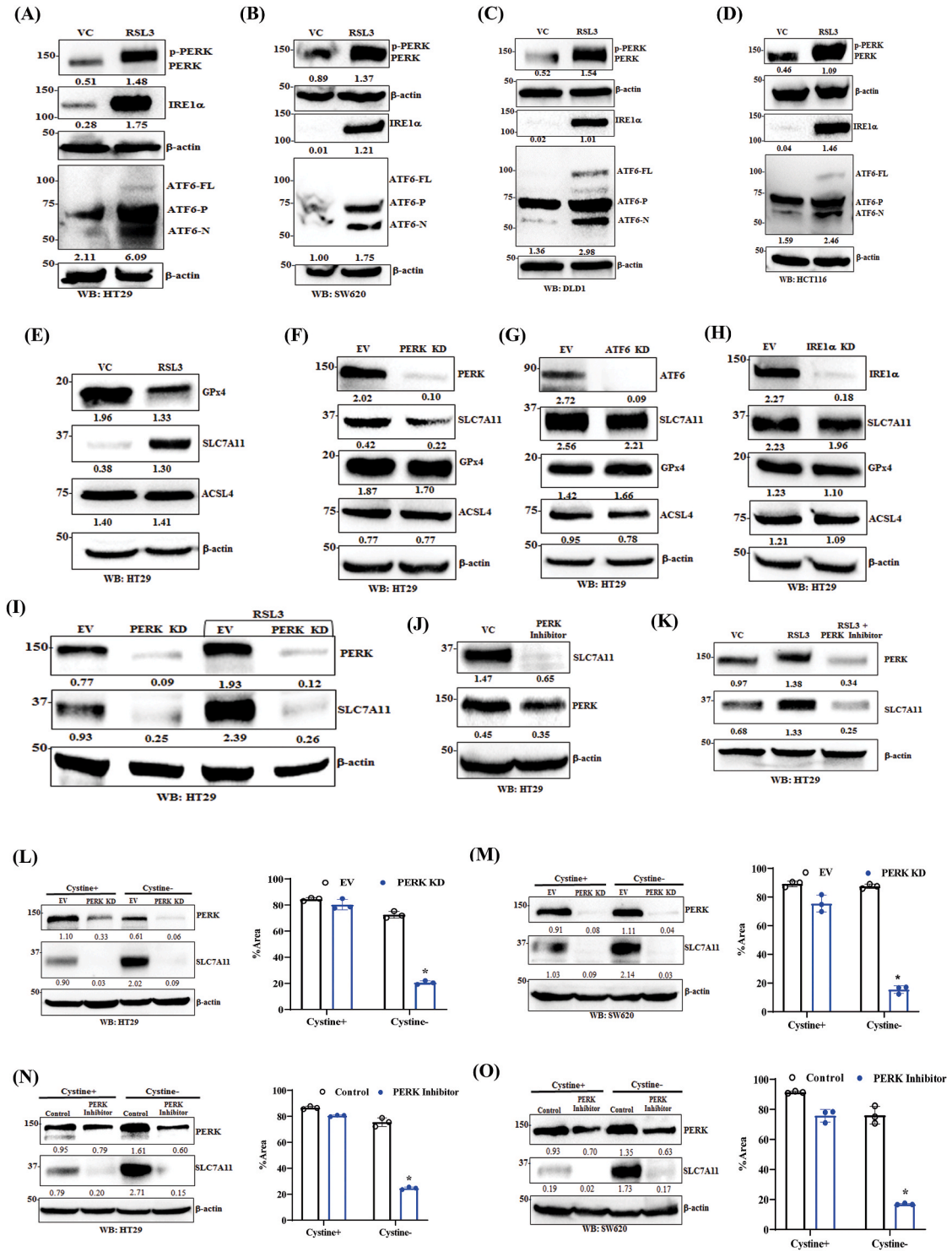

Fig. 1. Ferroptosis inducer RSL3 causes UPR and the PERK arm of UPR regulates SLC7A11 expression
(A-D) HT29, SW620, DLD1 and HCT116 cells were either treated with 1 μM RSL3 or vehicle control (VC) for 24 h and protein lysates were prepared for Western blot analysis. Immunoblot shows the expression for classical UPR marker proteins, i.e., PERK, ATF6, and IRE1α. Full-length ATF6 (ATF6-FL), membrane-associated ATF6 (ATF6-P), and nuclear-translocated S2P-cleaved ATF6 (ATF6-N) all are indicated in the immunoblot. (E) Major ferroptosis regulator proteins GPx4, SLC7A11, and ACSL4 in HT29 cells. (F–H) Immunoblot analysis of PERK, ATF6, IRE1α, SLC7A11, GPx4, and ACSL4 in (F) PERK knockdown (KD), (G) ATF6 KD and (H) IRE1α KD in HT29 cells with respective empty vector (EV). (I) Immunoblot showing the expression of PERK and SLC7A11 in EV and PERK KD HT29 cells that were either treated with vehicle or 1 μM RSL3 for 6 h. (J–K) Immunoblot analysis of PERK and SLC7A11 in (J) VC and 5 μM PERK inhibitor (GSK2656157) treated and (K) VC, PERK inhibitor and RSL3 treated HT29 cells. (L–M) EV and PERK KD, (N–O) VC and PERK inhibitor treated HT29 (L, N) and SW620 (M, O) cells were cultured in RPMI 1640 in the presence (cystine+) or absence (cystine-) of cystine for 72 h and subjected to Western blot analysis (left) for the expression of PERK and SLC7A11, quantitative analysis (right) of percent area covered by the cultured cells are shown in the graph (Original photomicrographs are shown in Supplementary Fig. 5). *p < 0.05; compared to control. β-actin was used as a loading control in all immunoblot studies. Respective molecular weight marker (left of each immunoblot) and densitometric quantifications (bottom of each immunoblot) are shown.

2

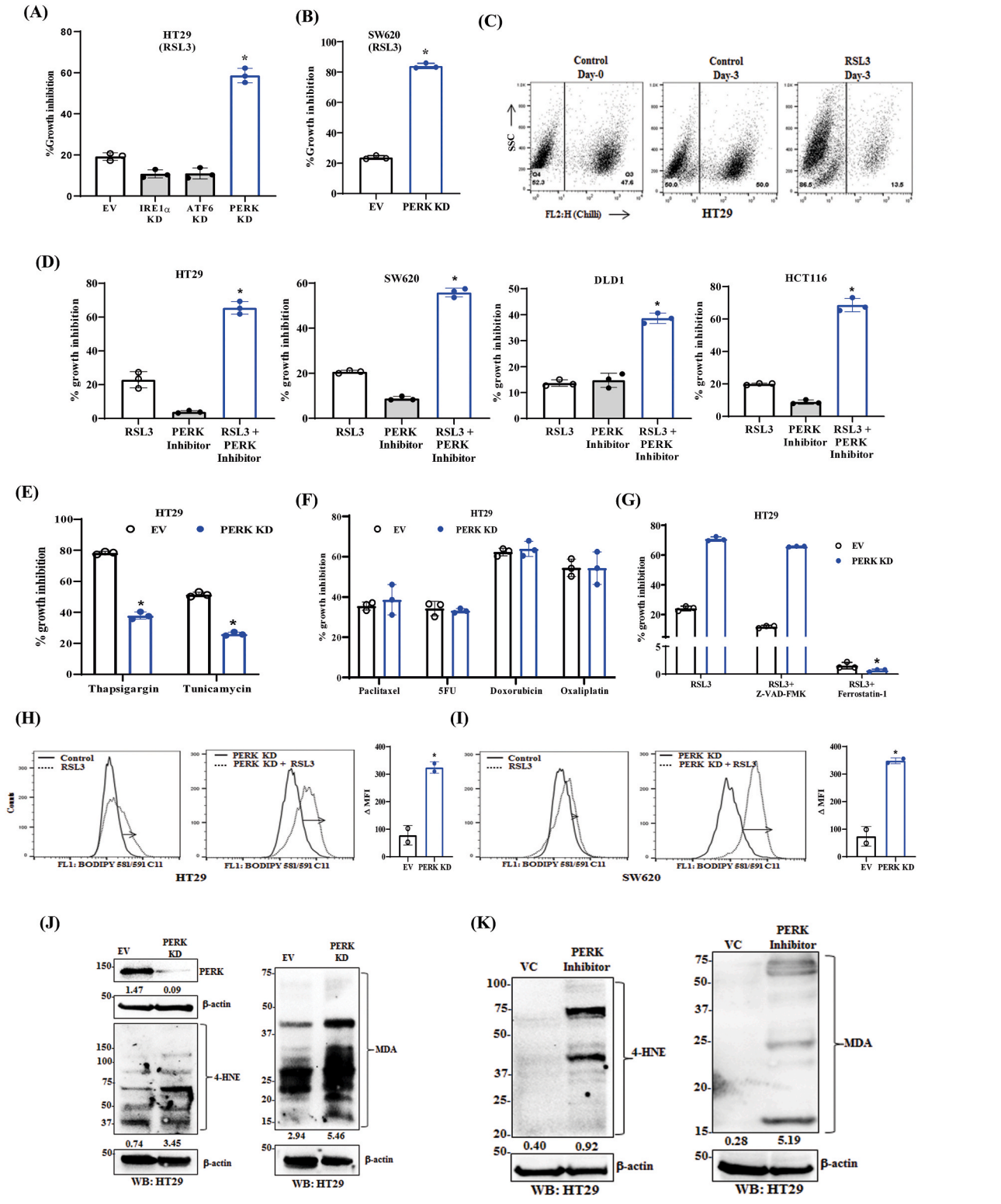

(caption on next page)

bottom panel). We treated HT29 cells with erastin, another potent ferroptosis inducer, and observed sensitization in PERK knockdown cells compared to the control (Supplementary Fig. 7). To further confirm the above observations, we seeded equal numbers of untagged HT29 EV (white) and chilli-luc tagged PERK (red) knockdown cells and cultured in the absence and presence of RSL3 for 3 days. FACS analysis of Day

Fig. 2. Loss of PERK function promotes ferroptosis in colorectal cancer
(A) HT29 EV, PERK, ATF6, and IRE1α KD cells were treated with either vehicle or 1 μM RSL3 for 48 h, and SRB assay was performed to evaluate the cytotoxic effect of the same. (B) SW620 EV and PERK KD cells were treated with vehicle or 1 μM RSL3 for 48 h, and subjected to SRB assay. For A and B, percent growth inhibition was tabulated. *$p < 0.05$; compared to respective EV. (C) HT29 EV (untagged) and chilli-tagged PERK KD (red) cells were mixed in equal numbers and subjected to flow cytometric analysis on day 0 and day 3 following treatment with vehicle control or 500 nM RSL3. Analysed cell populations are shown in the FACS plot. (D) Different CRC cells were treated with RSL3 (HT29 and SW620 - 1 μM), (DLD1 - 125 nM), and (HCT116 - 2 μM) alone or in combination with 5 μM of PERK inhibitor (GSK2656157) for 48 h and SRB assay was performed. Percent growth inhibition was tabulated. *$p < 0.05$; compared to RSL3 treated cells. (E) HT29 cells were treated with vehicle control or 10 nM Thapsigargin or 1 μg/ml Tunicamycin for 48 h and subjected to SRB assay. Percent growth inhibition was calculated and tabulated in columns. *$p < 0.05$; compared to respective controls. (F) HT29 EV and PERK KD cells were treated with vehicle control or different chemotherapeutic drugs i.e., paclitaxel (20 nM), 5-Fluorouracil (100 μM), Doxorubicin (10 μM), Oxaliplatin (50 μM) for 48 h and cytotoxic impact of these drugs was evaluated via SRB assay. Percent growth inhibition was tabulated in the columns. (G) HT29 EV and PERK KD cells were treated either with either 1 μM RSL3 alone or in combination with (25 μM) Z-VAD-FMK (pan-caspase inhibitor) or (10 μM) ferrostatin-1 (ferroptosis inhibitor) and percent growth inhibition in different groups was estimated by SRB assay. *$p < 0.05$; compared to respective RSL3 control. In A-B and D-G Columns represent an average of triplicate readings of samples; error bars ± S.D. (H–I left panel) Control (EV) and PERK KD of (H) HT29 and (I) SW620 cells were treated with 1 μM RSL3 or vehicle control for 24 h followed by BODIPY C11 staining (Lipid peroxidation sensor) and cells were analysed by FACS (detailed description provided in materials and methods section). Histogram overlays show BODIPY C11 positivity correlating with lipid peroxidation levels in respective groups. (H–I) Right Panels, respective delta mean fluorescence intensity (MFI) of the cells, stained for BODIPY C11. The delta mean was calculated by subtracting the mean fluorescence intensity of the control from the RSL3 treated cells. Columns represent an average of duplicate readings of samples; error bars ±S.D. *$p < 0.05$; compared to EV (control). (J–K) Immunoblots representing 4-Hydroxynonenal (4-HNE) and malondialdehyde (MDA) conjugated protein expression in (J) HT29 EV and PERK KD cells and (K) HT29 VC and PERK inhibitor-treated (24 h) cells. β-actin was used as a loading control in all immunoblot studies. Respective molecular weight marker (left of each immunoblot) and densitometric quantifications (bottom of each immunoblot) are shown. (For interpretation of the references to color in this figure legend, the reader is referred to the Web version of this article.)

0 and Day 3 cells shows a marked reduction of chilli luc tagged PERK (red) knockdown cells compared to untagged white control cells, again suggesting that loss of PERK sensitizes HT29 cells to cytotoxic function of RSL3 (Fig. 2C). Similar with the above findings, PERK inhibitor treatment markedly sensitizes RSL3 induced colon cancer cell (HT29, SW620, DLD1 and HCT116) death (Fig. 2D and Supplementary Fig. 8). To understand the selectivity of PERK function in sensitizing the actions of other ER stress inducers, control and PERK knockdown cells were treated with Thapsigargin and Tunicamycin and observe that both the ER stress inducers failed to deliver their cytotoxic effect in absence of PERK, instead of its sensitization impact that was seen earlier in case of RSL3 (Fig. 2E). Next to understand the clinical significance of this sensitization, we treated control and PERK knockdown HT29 and SW620 cells with classical chemotherapeutic drugs like paclitaxel, 5-fluorouracil and oxaliplatin and assessed their combined cytotoxic potential. Unfortunately, again we did not observe any synergistic cytotoxic effect on any of the chemotherapeutic drugs in combinations with PERK loss of function (Fig. 2F, Supplementary Figs. 9 and 10). The above findings suggest that sensitization observed by PERK knockdown is specific to RSL3. Next, we sought to determine whether RSL3-mediated sensitization of cell death in the loss of PERK function is due to the induction of apoptosis or ferroptosis. To find out the same, we treated PERK knockdown cells with RSL3 in the presence or absence of either apoptosis inhibitor (pan-caspase inhibitor Z-VAD-FMK) or ferroptosis inhibitor (ferrostatin-1) and observed that only ferroptosis inhibitor (ferrostatin-1) significantly rescues cytotoxic impact of RSL3 (Fig. 2G). The above findings demonstrate the role of ferroptosis in PERK knockdown-mediated sensitization of cell death. Additionally, there was no significant difference in cell growth inhibition with RSL3 along with pan-caspase inhibitor, so classical apoptotic cell death has a minimal role associated with RSL3-induced cell death. Ferroptosis is distinct from other types of programmed cell death and is characterised by the accumulation of lipid peroxides that can be detected by BODIPY-C11 staining of cells [35] To check the level of lipid peroxidation after RSL3 treatment, we treated HT29 (Fig. 2H, left and right panel) and SW620 (Fig. 2I, left and right panel) EV and PERK knockdown cells with RSL3 for 24 h and subjected them to BODIPY-C11 staining (details described in materials and methods), we observe a marked increase in excitation shift of BODIPY-C11 staining in PERK knockdown cells as compared to control, suggesting that loss of PERK promotes lipid peroxidation and ferroptosis in colorectal cancer cells. 4-HNE and MDA are known lethal by-products of lipid peroxidation or ferroptosis, formed during the enzymatic and non-enzymatic breakdown of AA (arachidonic acid) and other PUFAs (polyunsaturated fatty acids) [36,37]. Here, we assessed the expression of 4-HNE and MDA in HT29 control, PERK KD and PERK inhibitor-treated cells and found their robust upregulation in both PERK KD (Fig. 2J) and PERK inhibitor (Fig. 2K) treated cells as compared to respective controls. PERK kinase activity inhibition in other CRC cell lines (SW620, DLD1 and HCT116) showed similar upregulation of these ferroptosis biochemical markers as compared to their respective controls (Supplementary Fig. 11). The above observations highlight the importance of PERK as a negative ferroptosis regulator in colorectal cancer and suggest that apoptotic cell death has a minimum role in PERK mediated ferroptosis modulation. The above experimental evidence suggested us to dig deeper into the mechanistic aspects of PERK-mediated SLC7A11 regulation and ferroptosis induction.

2.3. *PERK regulates the expression and recruitment of transcription factor ATF4 to the promoter of SLC7A11 in the course of ferroptosis modulation*

RSL3-mediated upregulation of UPR-responsive proteins and further PERK mediated robust upregulation of SLC7A11 protein expression in RSL3 treatment prompted us to evaluate the impact of RSL3-mediated gene regulation at transcriptional level. We evaluated mRNA expression of UPR marker genes i.e., *PERK, ATF6* and *IRE1a* and *SLC7A11* in HT29 cells (vehicle control and RSL3 treatment) and observed that all three UPR marker genes (Fig. 3A) and SLC7A11 (Fig. 3B) were found to be highly upregulated in RSL3 treated cells as compared to control. RSL3 mediated robust induction of PERK mRNA expression justifies its protein overexpression following RSL3 treatment. Next, we wanted to determine RSL3 mediated PERK activation is a direct RSL3 effect or indirect via the RSL3 mediated induction of ferroptosis. To investigate such possibilities, we treated cells with RSL3 alone and in combination with ferroptosis inhibitor Ferrostatin-1 (FER-1) and assessed the activation status of PERK and its downstream proteins. As shown in Fig. 3C, RSL3 treatment promotes robust PERK activation or phosphorylation (as determined by upper shift of PERK band) along with overexpression of GRP78 and ATF4. However, the whole RSL3 mediated PERK and downstream activation was found to be completely abrogated when the cells are pre-treated with FER-1. Therefore, RSL3-mediated ferroptosis induction or lipid peroxidation promotes PERK phosphorylation and its downstream signals. To further confirm the positive regulatory loop between PERK and SLC7A11, we utilized Thapsigargin to activate the whole pathway and then assessed the impact of PERK inhibitor on SLC7A11 modulation. As shown in Fig. 3D, PERK inhibitor treatment completely mitigated Thapsigargin induced PERK activation, SLC7A11, and ATF4 induction. As ATF4 is a critical downstream transcription factor of *PERK*, we further determined the level of ATF4 protein in control and PERK knockdown cells and found that level of ATF4, as well as SLC7A11, are markedly downregulated in PERK knockdown cells as compared to

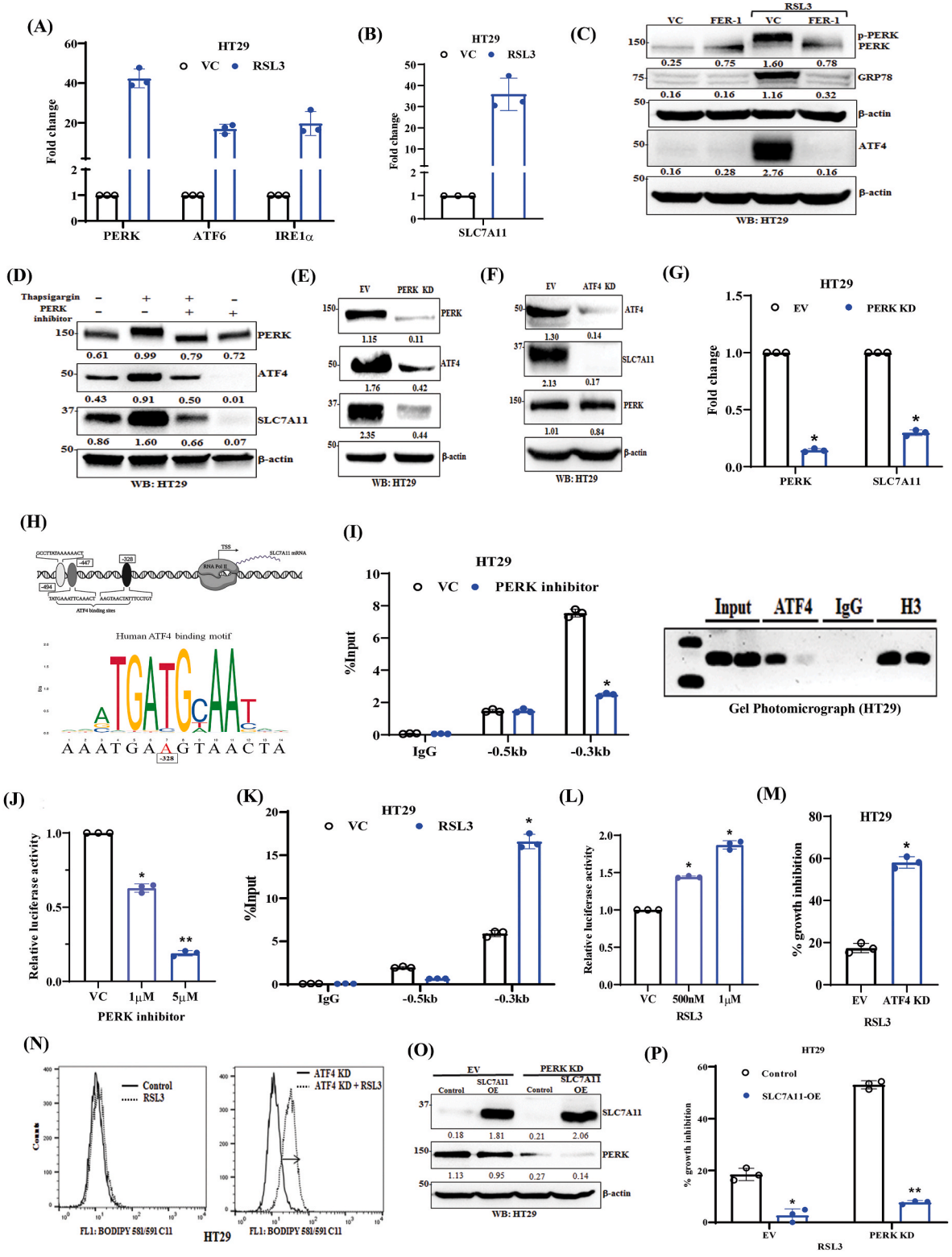

(caption on next page)

control (Fig. 3E). Moreover, to understand the direct regulation of ATF4 on SLC7A11 expression, we made stable knockdown of ATF4 in HT29 cells and observed that SLC7A11 protein expression is robustly down-regulated in ATF4 knockdown cells as compared to control (Fig. 3F).

Because *ATF4*, a major PERK downstream transcription factor, is downregulated in PERK KD conditions, we decided to investigate the role of PERK in *SLC7A11* transcriptional regulation. First, we observed that PERK knockdown severely reduces mRNA expression of *SLC7A11* in

Fig. 3. PERK-ATF4 axis regulates *SLC7A11* expression and colorectal cancer cell ferroptosis
(A) Total RNA was isolated from control and RSL3 treated HT29 cells, reverse transcribed, and subjected to qRT-PCR analysis for *PERK, ATF6* and *IRE1α* mRNA expression. Fold change in mRNA expression is represented in the bar graph. Data is representative of three independent experiments, resulting from different samples; Columns, the fold change of mRNA expression of *PERK, ATF6* and *IRE1α* compared to respective control. (B) Control and RSL3 treated HT29 cells were subjected to qRT-PCR analysis as described above for expression of the *SLC7A11* gene. Columns represents fold change in mRNA expression of *SLC7A11*; bars ±SD. *, $p < 0.05$, compared with control. (C) HT29 cells were pre-treated for 30 min with 10 μM Ferrostatin-1 (ferroptosis inhibitor) and further treated with 1 μM RSL3 alone or in combination with FER-1. Immunoblot analysis shows the expression of PERK, Bip/GRP78, and ATF4. (D) HT29 cells were treated with Thapsigargin (ER stress inducer) alone or with PERK inhibitor (pre-treated for 2 h) for 6 h and subjected to Western blot analysis. The expression of PERK, ATF4, and SLC7A11 is shown in the immunoblot images. (E–F) Immunoblots show the expression of PERK, ATF4, and SLC7A11 in (E) HT29 EV and PERK KD or (F) HT29 EV and ATF4 KD cells. (G) qRT-PCR analysis of HT29 EV and PERK KD cells; Columns showing the fold change in mRNA expression of *PERK* and *SLC7A11* genes. bars ±SD. *, $p < 0.05$, compared with respective control. (H) Diagrammatic representation of *SLC7A11* promotor showing (Top) putative ATF4 DNA binding sites and transcription start site (TSS) with RNA pol II, (Down) Human ATF4 binding motif of *SLC7A11* promoter on predicted binding site (-0.3 kb upstream from TSS) that is publicly available at JASPAR database (http://www.jaspar.genereg.net). (I) ChIP assay (Details described in the Methods section) was performed in vehicle control, and PERK inhibitor-treated (24 h) HT29 cells using anti-ATF4 and IgG antibodies and then examined by real-time qPCR using primer pairs targeting predicted -0.3 kb and -0.5 kb ATF4 binding sites upstream from TSS of the *SLC7A11* gene. Fold change in enrichment for ATF4 and IgG with respect to % input was shown; Data is representative of three independent experiments resulting from different samples; Columns, the average value of percentage enrichment compared to input; bars ±SD. *, $p < 0.05$, compared with respective control. Photomicrograph of Gel showing conventional PCR validation of ChIP experiments. Lanes are vehicle control and treatment, respectively, for each group of the ChIP sample. (J) The HEK293 cells were transfected with -0.6 kb upstream of *SLC7A11* promoter luciferase construct plasmid (pGL4.12) followed by treatment with vehicle or 1 μM and 5 μM of PERK inhibitor for 24 h and cells were harvested for luciferase activity (detailed description in Methods Section). Columns, the average value of relative firefly luciferase activity compared to Renila luciferase activity derived from triplicate readings of different samples; bars ±SD. **, $p < 0.01$, compared with vehicle control. (K) HT29 cells were treated with vehicle control or 1 μM of RSL3, and ChIP assay was performed using anti-ATF4 and IgG antibodies and then examined by real-time qRT-PCR using primer pairs targeting the predicted ATF4 binding sites on the *SLC7A11* promoter. Fold change enrichment for ATF4 and IgG with respect to % input was shown in Columns; bars ±SD. *, $p < 0.05$, compared with vehicle control. (L) The HEK293 cells were transfected with -0.6 kb upstream of *SLC7A11* promoter luciferase construct plasmid, followed by treatment with vehicle or 500 nM and 1 μM of RSL3 for 24 h, and subjected to luciferase activity. Columns, the average value of relative firefly luciferase activity compared to Renila luciferase activity derived from triplicate readings of different samples. (M) HT29 EV and ATF4 KD cells were treated with 1 μM RSL3 for 48 h, and SRB assay was performed. Percent growth inhibition was tabulated, Columns, an average of triplicate readings of samples; error bars ±S.D. *$p < 0.05$; compared to EV. (N) HT29 EV and ATF4 KD cells were treated with 1 μM RSL3 for 6 h and analysed by flow cytometry after staining with BODIPY C11. Histogram overlays show lipid peroxidation levels in respective treatment groups. (O) EV and PERK KD HT29 cells were made stable for overexpression of SLC7A11 and subjected to immunoblot analysis for SLC7A11 and PERK. (P) HT29 EV and PERK KD cells with stable SLC7A11 overexpression (as shown in the immunoblot) were treated with 1 μM RSL3 for 48 h and subjected to SRB assay. Percent growth inhibition was tabulated, Columns, an average of triplicate readings of samples; error bars ±S.D. *$p < 0.05$; compared to respective control. β-actin was used as a loading control in all immunoblot studies. Respective molecular weight marker (left of each immunoblot) and densitometric quantifications (bottom of each immunoblot) are shown.

HT29 colorectal cancer cells, as observed in Fig. 3G. Further, we wanted to evaluate the contribution of ATF4 recruitment in PERK mediated downregulation of SLC7A11 expression. As shown in Fig. 3H, the *SLC7A11* promoter has three putative ATF4 binding sites predicted by the publicly available software Eukaryotic Promoter Database (https://epd.epfl.ch/). In our ChIP assay (Fig. 3I), we observed marked selective enrichment of ATF4 at the -0.3 kb site upstream of the *SLC7A11* promoter in control cells, which was found to be significantly reduced following PERK inhibitor treatment. Loss of ATF4 recruitment at the *SLC7A11* promoter following PERK inhibition prompted us to check its role in modulating *SLC7A11* transcription. In our dual luciferase assay, we transfected the SLC7A11 promoter luciferase construct in HT29 cells (-0.6 kb from the TSS, cloned in the luciferase assay reporter vector pGL4.12), and found that PERK inhibitor reduces SLC7A11 transcription (relative luciferase activity) in a dose-dependent manner (Fig. 3J). The above data suggest that ATF4 functions as a transcription factor in PERK mediated regulation of *SLC7A11* expression. To further confirm the above hypothesis, we performed ChIP assay in HT29 cells and found that RSL3 treatment increased the enrichment of ATF4 on the predicted binding site at the SLC7A11 promoter (Fig. 3K). Further, as observed in dual luciferase assay, RSL3 treatment induces SLC7A11 transcriptional activity in a dose-dependent manner in HT29 cells (Fig. 3L). To assess the phenotypic impact of the PERK-ATF4-SLC7A11 axis, we treated control and ATF4 KD cells with RSL3 and performed cell viability assay and BODIPY C11 staining. As observed in Fig. 3M, ATF4 loss not only makes cells prone to death in response to RSL3 but also promotes increased ferroptosis compared to control (Fig. 3N). Altogether, our experimental results clearly indicate that PERK regulates ferroptosis through *SLC7A11* expression by modulating the recruitment of ATF4 to its promoter. To further evaluate the phenotypic role of System Xc^- in the hypersensitivity of PERK loss of function toward RSL3 in CRC cells, we ectopically overexpressed SLC7A11 in HT29 EV and PERK KD cells (Fig. 3O) and determined cytotoxic response of RSL3 in those conditions. As shown in Fig. 3P, both EV and PERK KD HT29 cells become significantly resistant to RSL3 mediated ferroptotic cell death following ectopic overexpression of SLC7A11. The above observation suggests that SLC7A11 or System Xc^- is a major player in PERK driven ferroptotic process.

2.4. Loss of PERK inhibits tumor growth and demonstrates active signs of ferroptotic tumor cell death in vivo

Considering the above-mentioned findings, we sought to look into the influence of PERK knockdown on tumor progression in vivo. We inoculated EV (control) and PERK KD HT29 cells ($2x10^6$ respectively) subcutaneously in nude mice and monitored the tumor progression twice a week for up to 6 weeks. As observed in Fig. 4A-4C, compared to the control, PERK KD resulted in a marked reduction of tumor volume (Fig. 4A, 4B) and weight (Fig. 4C). Further, we performed Western blot analysis of the harvested tumors to investigate the effect of PERK loss of function on the expression of SLC7A11 and ATF4 as well as hallmark ferroptotic markers such as 4-HNE and MDA in vivo. As observed in Fig. 4D, PERK knockdown is maintained in vivo tumors and loss of PERK strongly reduces SLC7A11 expression along with ATF4 but promotes marked expression of both ferroptotic markers such as 4-HNE and MDA. We performed immunohistochemistry (IHC) staining using MDA and 4-HNE antibodies in control and PERK knockdown tumors to further validate the above finding. We observed that compared to the control, PERK KD tumors display robust overexpression of 4-HNE and MDA (Fig. 4E). Further, we have calculated the IHC ATM (Averaged Threshold Measure) score by measuring the DAB intensity in respective IHC images, as represented in Fig. 4F–4G, where we find that PERK KD tumors have robustly high ATM scores for both 4-HNE and MDA staining as compared to the control tumor. Together, our data indicate that PERK has an immense impact on tumor growth and genetic inhibition of PERK results in significant loss of tumor growth, along with the elevated levels of 4-HNE and MDA proteins. This suggests active ferroptotic tumor cell death in the course of PERK mediated tumor growth reduction.

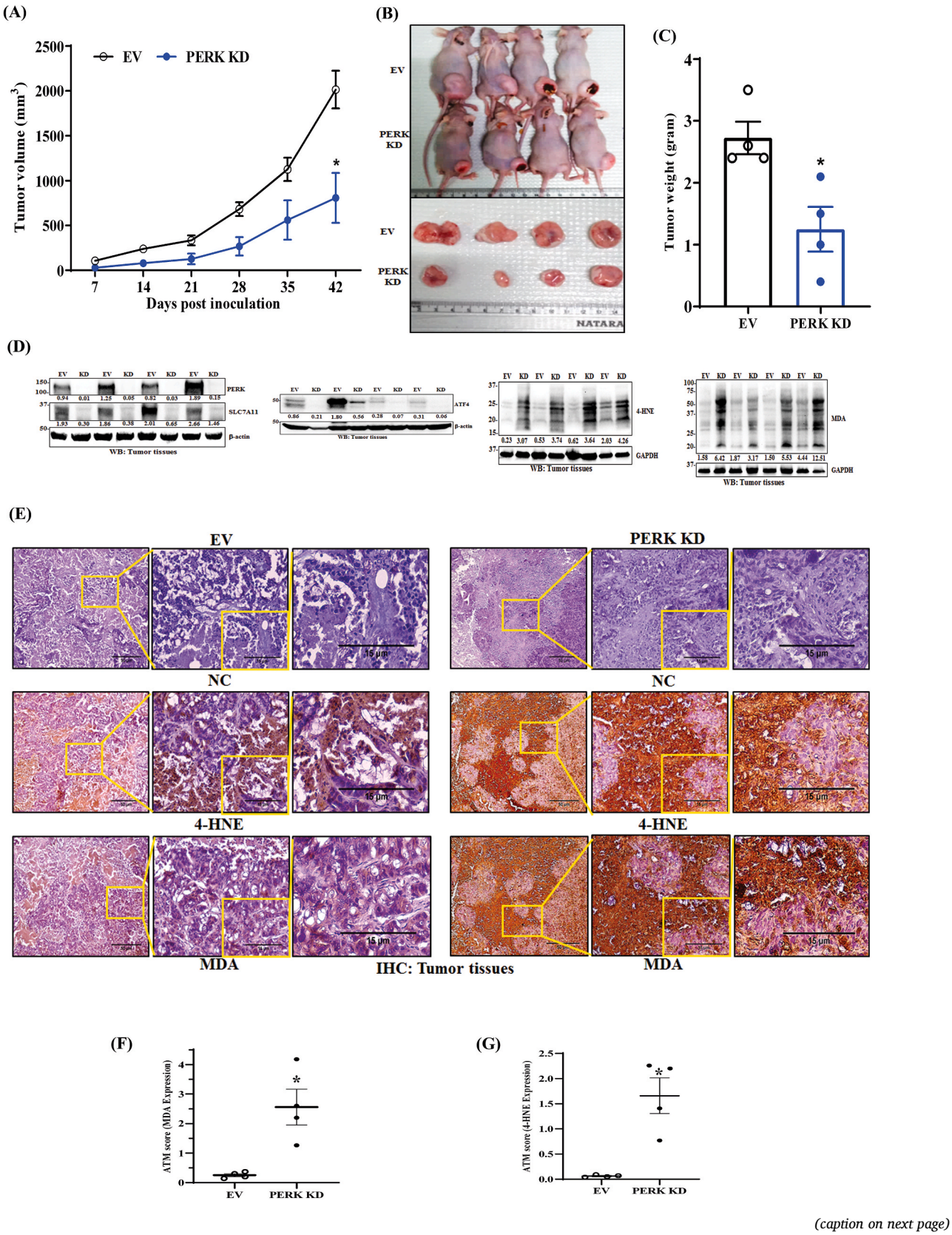

(caption on next page)

Fig. 4. Loss of PERK has compromised in vivo colorectal tumor growth due to increased ferroptosis
2 x 10^6 HT29 EV and PERK KD cells in 100 μl PBS were injected subcutaneously in the flanks of the right hind leg of 4–6 weeks old Crl: CD1-Foxn1nu mice in two different groups for each condition. Tumor volumes were measured twice a week with a caliper. (A) Tumor progression of the same is shown in the graph. Each point indicates the average tumor volumes at a particular time; error bars ± SEM (n = 4 for each group); *p < 0.05 compared to control tumors. (B) Photographs of tumor-bearing mice (top) and harvested tumors (bottom) from respective groups were shown. (C) The average tumor weight of each group is shown in the graph. error bars ± SEM (n = 4 for each group); *p < 0.05 compared to control tumors. (D) Harvested tumors were lysed and subjected to Western blot analysis to visualize the protein expression of PERK SLC7A11, ATF4, MDA (malondialdehyde) and 4-HNE (4-Hydroxynonenal). β-actin and GAPDH were used as loading control in immunoblot studies. Respective molecular weight marker (left of each immunoblot) and densitometric quantifications (bottom of each immunoblot) are shown. Respective molecular weight marker (right) and densitometric quantifications (below) are shown for respective blots of all Western blot images. (E) Immunohistochemistry was conducted to detect MDA and 4-HNE in formalin-fixed paraffin-embedded serial sections of harvested tumors with respective antibodies. Representative photomicrographs are shown at 10X and 40X magnifications. Scale bar, 50 μm (10X) or 15 μm (40X). (F–G) Quantitative ATM scores for the expression of (F) MDA and (G) 4-HNE are represented as scatter plots; Error bar, +/- SEM, *p-value, <0.05, compared to expression in control tumors.

2.5. Expression of PERK and SLC7A11 is positively correlated in human colorectal cancer

To draw a clinical correlation between *PERK* and *SLC7A11* expression, we performed TCGA data mining using the UCSC Xena browser (https://xenabrowser.net/). We accessed mRNA expression data of 471 patients in the GDC TCGA COAD cohort of the database and drew a correlation plot between *PERK* and *SLC7A11* expression, and calculated Pearson's correlation (R), where we found a positive correlation between *PERK* and *SLC7A11* expression (Fig. 5A). Further, we confirmed a positive correlation between *PERK* and *SLC7A11* expression in 15 human colorectal cancer patients by performing Real-Time-PCR analysis of CRC tumors and their respective matched normal counterparts (Fig. 5B). As shown in Fig. 5C-5D, we find that both PERK and SLC7A11 are overexpressed in human CRCs compared to normal counterparts.

The graphical abstract (Fig. 5E) summarises how selectively the PERK arm of ER stress/UPR protects cancer cells from ferroptosis. PERK mediated ATF4 upregulation and ATF4 binding to the promoter of *SLC7A11* results in upregulation of System Xc^- that stimulates cystine import into the cytosol and inhibits lipid peroxidation and ferroptosis.

3. Discussion

Cancer cells make themselves resistant to therapeutic insults by effectively managing UPR and ER stress responses. It has been well established in the literature how an apoptotic stimulus induces ER stress in cancer cells leading to the activation of UPR and determination of the final cell fate decisions [38–40]. Recent reports also indicated the close connectivity between ferroptosis induced ER stress and crosstalk among ferroptosis and apoptosis [34,41]. Here, our study highlights that ferroptosis inducers can cause UPR and ER stress in colorectal cancer cells, where PERK arm of UPR selectively plays a decisive role in modulating ferroptotic response [42]. In corollary with our findings, ferroptosis inducers like Sorafenib, Dihydroartemisinin (DHA), Erastin, and 4-HNE (a by-product of lipid peroxides) have also shown to induce ER stress and UPR downstream signaling modulators. These modulators like ATF4, NRF2 GRP78 have been shown to prevent ferroptosis in different settings including cancer [11,43–49]. Besides multiple reports demonstrating the involvement of the PERK arm of UPR in modulating apoptosis and autophagy, recent findings by Zheng et al. showed that PERK mediated sensitization of hepatocellular carcinoma in response to irradiation is due to enhanced apoptosis or ferroptosis [50]. In prostate cancer, it has been shown that loss of ATF6α promotes ferroptotic cell death, though the contribution of the other two arms (PERK and IRE1α) was not explored in this process [51]. In the current study, we observe the selective participation of PERK, over the other two UPR arms, in modulating ferroptosis. An elegant study by Chen et al., earlier demonstrated that inhibition of the PERK-ATF4-HSPA5-GPX4 pathway increased DHA sensitivity of glioma cells by increasing ferroptosis, where they did not observe significant change in SLC7A11 level [46]. We observe similar upstream changes in response to RSL3 or loss of PERK function, but alterations in SLC7A11 level turn out to be the key factor for modulating ferroptotic phenotype in colon cancer. Our differential observations hint towards a possible contribution of context dependency and cancer specificity. Another unique aspect of our finding is that we observe exclusive ferroptotic cell death induction in the absence of PERK, which could only be rescued by ferroptosis inhibitor ferrostatin-1, and not by any other inhibitors of apoptosis and autophagy. This essentially advocates that the possibility of cross-talk between PERK mediated ferroptosis versus autophagy and apoptosis is minimal when the upstream signals come from lipid peroxidation. In fact, any of the chemotherapeutics tested in our study failed to sensitize colorectal cancer to either apoptosis or ferroptosis in the absence of PERK. This further supports the exclusivity of PERK in modulating the ferroptotic process. In addition to this, PERK has been shown to be selectively activated during Epithelial-to-Mesenchymal Transition (EMT) process, making cancer cells vulnerable to ER stress [52].

GPX4, SLC7A11 and ACSL4 are major downstream effectors of any ferroptotic process and the intricate balance between these play a critical role in executing full-blown ferroptosis [7,53,54]. For example, the presence of PERK in the cancer cells prevents the ferroptotic impact of GPX4 inhibitor RSL3 by positively regulating the expression of SLC7A11. Though the ferroptosis perspective was not studied, following exposure to paclitaxel, cancer cells have been shown to activate the PERK-ATF4 axis and maintain redox homeostasis by inducing the expression of the major antioxidant enzymes, including SLC7A11 [55]. Several studies have indicated the regulation of *SLC7A11* by ATF4, but our study, for the first time, provided direct evidence for the transcriptional regulation of *SLC7A11* via ATF4 binding to its promoter [56,57]. In support of our observations, ATF4 has been shown to drive resistance to Sorafenib in hepatocellular carcinoma by preventing ferroptosis [58].

It is noteworthy to mention that in in vitro condition, functional loss of PERK either through PERK knockdown or by the treatment of PERK inhibitor alone does not result in ferroptotic cell death but loss of PERK function primes colorectal cancer cells towards ferroptosis which is evident by increased expression of 4-HNE and MDA in PERK knockdown state. However, in in vivo condition, we observe that PERK knockdown in colorectal cancer cells alone is able to reduce tumor growth significantly and harvested tumors show robust positivity for ferroptosis markers like 4-HNE and MDA. The above results advocate that in in vivo condition under the influence of tumor microenvironment, PERK loss of function alone is sufficient to deliver its anti-tumor impact. Therefore, PERK inhibitors may have huge therapeutic potential in the clinics especially where tumors are non-responsive to chemotherapy that usually promotes apoptotic cell death.

Altogether, our study reveals a new role of the PERK-ATF4-SLC7A11 axis in modulating ferroptotic cell death in colorectal cancer in vitro and in vivo and posits therapeutic rationale for the development of small molecule PERK inhibitors against colorectal cancers that are commonly resistant to apoptosis but vulnerable to ferroptosis.

4. Materials and methods

4.1. Reagents and antibodies

Dimethyl Sulfoxide (DMSO), Doxorubicin, Paclitaxel, 5-fluorouracil,

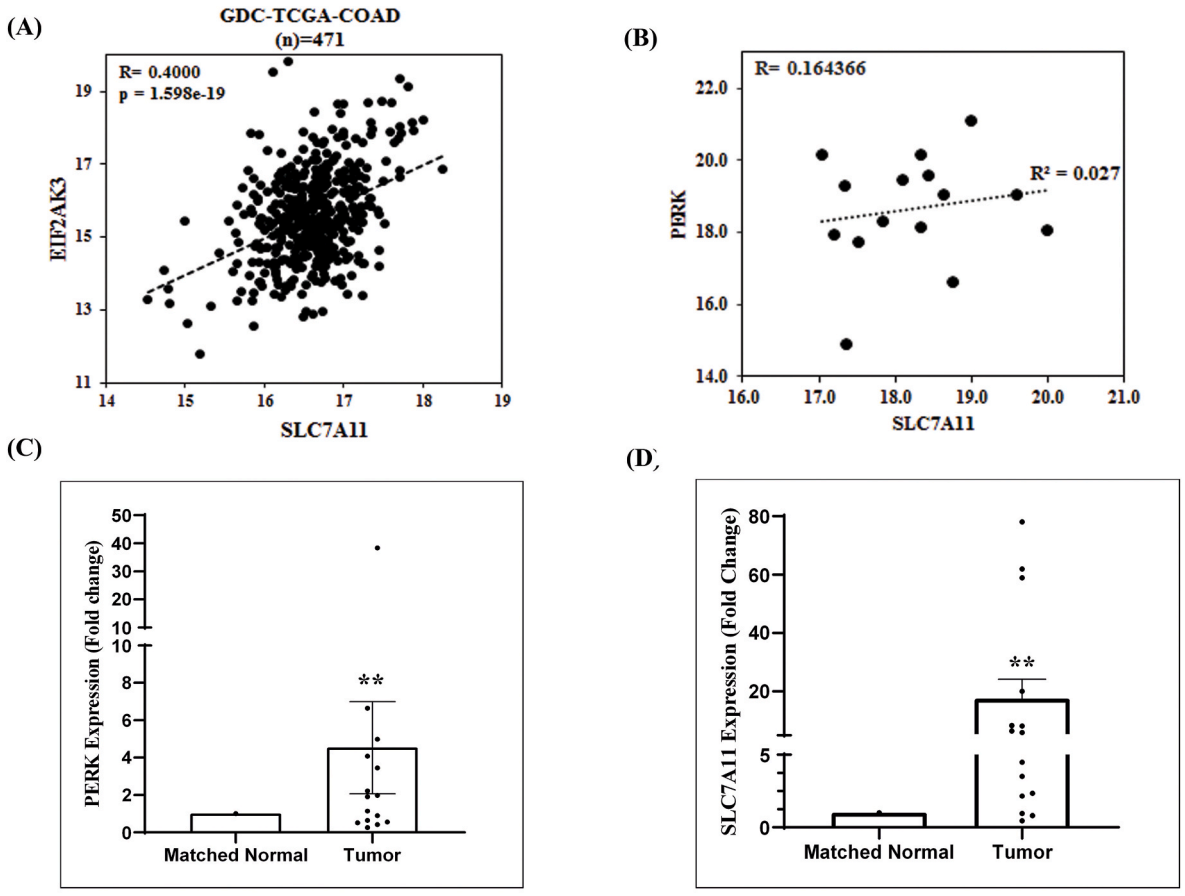

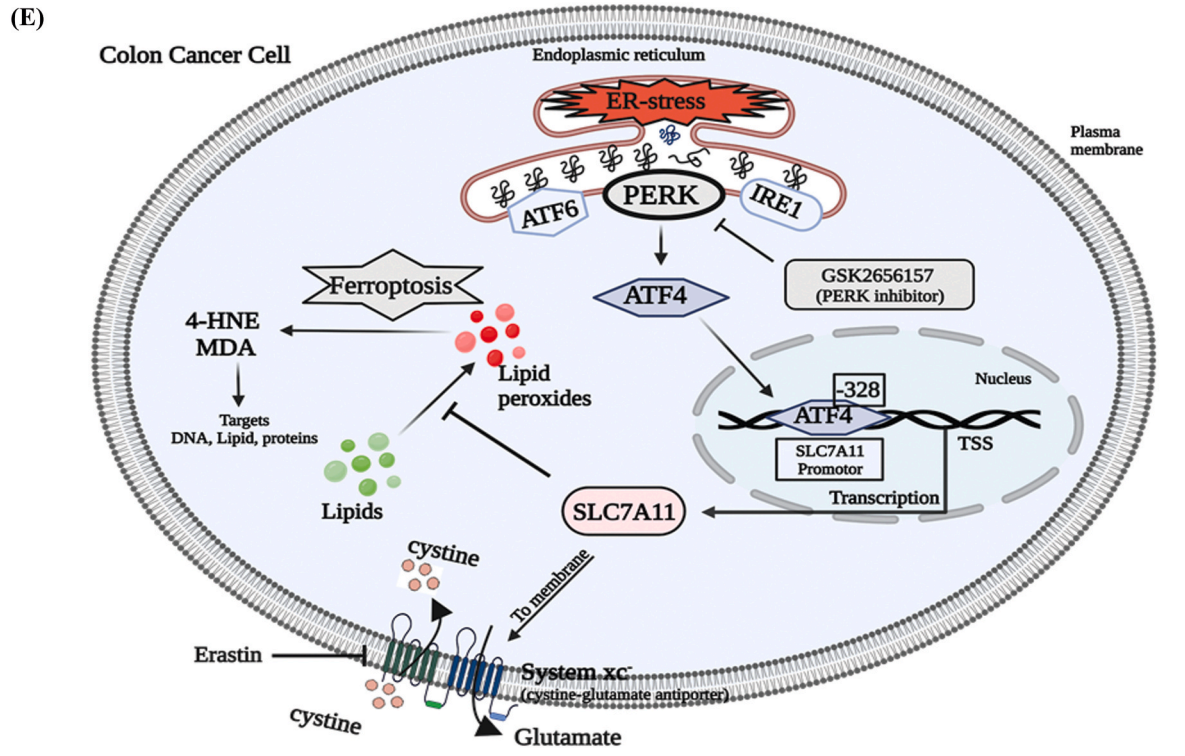

(caption on next page)

Fig. 5. PERK (*EIF2AK3*) and *SLC7A11* are positively correlated in human colorectal tumors
(A) GDC TCGA COAD patient data were acquired from the Xena browser, and a correlation graph was plotted between *EIF2AK3* (PERK) and *SLC7A11*. R (Pearson's correlation coefficient) (B) RT-PCR in matched non-malignant (Normal) and malignant tumor samples of colorectal cancer patients showed the correlation between delta Ct of *EIF2AK3* (PERK) and *SLC7A11*. (C–D) Total RNA was isolated from colorectal cancer patient tumor tissue samples along with their respective matched non-malignant counterparts, reverse transcribed, and RT-qPCR was performed for *PERK* and *SLC7A11* expression analysis. 18s is used as an internal control. Fold change in mRNA expression in (C) *PERK* and (D) *SLC7A11* is shown in bar diagram; Columns, the average value of fold change as compared to control; error bars ± SEM. *, $p < 0.05$, compared to control, $n = 15$. (E) The findings are illustrated in a graphical abstract showing how selectively PERK arm of ER stress regulates ferroptosis in colorectal cancer.

anti-β-Actin (cat#A3854) antibody, Doxycycline, Bovine Serum Albumin (BSA), Ferrostatin-1 (Fer-1), Thapsigargin, Tunicamycin and Polybrene were purchased from Sigma-Aldrich. RSL3 (cat#B6095) and Erastin (cat#B1524) were purchased from APExBIO. PERK inhibitor GSK2656157 (Cat#S7033) was purchased from Selleck Chemicals LLC. Recombinant Anti-Glutathione Peroxidase 4 antibody [EPNCIR144] (cat# ab125066) obtained from Abcam. Anti-ATF6α antibody clone# (37-1) (cat#73–505) was procured from BioAcademia. PVDF membrane and stripping buffer were obtained from Millipore Inc. BCA protein estimation kit, RIPA cell lysis buffer, blocking buffer, Super Signal West Pico and Femto chemiluminescent substrate, Lipofectamine-3000, Puromycin, FBS, RPMI-1640 media, Anti-Anti, were purchased from Thermo Fisher Scientific. Primers for real-time PCR and ChIP assay were purchased from IDT Inc and Eurofins Scientific. All chemicals were purchased from Sigma or Thermo scientific unless specified otherwise. Antibodies were obtained from cell signaling technology (CST) or mentioned otherwise.

4.2. Cell culture

Colorectal cancer cell lines HT29, SW620, DLD1, and HCT116 were obtained from American Type Culture Collection (ATCC), USA. Mycoplasma-free early passage cells were resuscitated from liquid nitrogen vapor stocks and inspected microscopically for stable phenotype before use. HT29, DLD1, and HCT116 cells were cultured in RPMI-1640 medium containing 10% fetal bovine serum (Gibco/Invitrogen), supplemented with anti-anti (Invitrogen containing 100 μg/ml streptomycin, 100 unit/ml penicillin, and 0.25 μg/ml amphotericin B). SW620 cells were cultured in DMEM medium containing 10% fetal bovine serum (Gibco/Invitrogen), supplemented with anti-anti. RPMI-1640 L-cysteine, L-cystine, L-glutamine and L-methionine free media (MP Biomedicals) was used to culture HT29 cells in cystine-free conditions. STR profiling was performed to authenticate all the cell lines employed in the investigation. Cell lines were cultured in an Eppendorf Galaxy 170R/170S CO2 incubator to provide a stable and homogeneous 5% CO_2 and 37°c temperature and humid atmosphere required for cell culture.

4.3. Cytotoxicity assay (SRB assay)

In-vitro cytotoxic effects of RSL3, Paclitaxel, Doxorubicin, 5-Fluorouracil, and Oxaliplatin were assessed with standard SRB (Sulforhodamine B) assay as described before [59,60]. Following an incubation period of 48 h, cell monolayers were fixed with 10% (wt/vol) trichloroacetic acid and stained for 30 min before being washed repeatedly with 1% (vol/vol) acetic acid to remove excess color. The protein-bound dye was dissolved in a 10 mM Tris base solution, and the absorbance of the treated and untreated cells was measured on a multi-well scanning spectrophotometer (Epoch Microplate Reader, Biotek, USA) at a wavelength of 510 nm. All the calculations for percent inhibition and IC50 were done in excel.

4.4. Western blotting

After harvesting, the cells or tissues were lysed on ice with Pierce™ RIPA lysis solution for 30 min. The Pierce™ BCA protein assay kit was used to estimate the protein concentration of the lysates. An equal quantity of the protein was resolved in a 4–15% Mini-PROTEAN® TGX™ Precast Protein Gels and transferred to an Immun-Blot PVDF Membrane (Bio-Rad) for antibody incubation. After transfer, the PVDF membrane was blocked with 5% non-fat dry milk or 5% BSA, followed by incubation with appropriate dilutions (manufacturer's protocol) of primary antibodies overnight at 4°C. After 3 washes for 5 min each, the membrane was incubated with a 1:5000 dilution of horseradish peroxidase-conjugated secondary antibody for 1 h at room temperature. Immunoreactivity was detected by enhanced chemiluminescence solution (Bio-Rad Clarity Western ECL Substrate and Immobilon™ western, Millipore, USA) and scanned by the gel documentation system (Bio-Rad chemidoc XRS plus).

4.5. Flow cytometry

We used flow cytometry to assess the cytotoxic effect of RSL3, Paclitaxel, Doxorubicin, 5-Fluorouracil, Oxaliplatin in HT29 EV (untagged) and PERK knockdown cells (pUltra-Chili-Luc-red). In brief, 6 lacs cells/well were seeded in 6-well plates and allowed to grow with treatment or vehicle control. Cells were harvested with TrypLE (Invitrogen) for single-cell suspension in FACS buffer (PBS with 0.1% BSA and 1 mM EDTA). After washing and centrifugation, cell pellets were resuspended in FACS buffer and analysed by FACS Calibur (BD). Acquired data were analysed using FlowJo software (Treestar).

4.6. BODIPY 581/591 C11 assay

BODIPY 581/591 C11 (Invitrogen) is a lipid-soluble fluorescent indicator of lipid peroxidation. Upon oxidation, its excitation maximum shifts from 581 to 500 nm, and the emission maximum shifts from 591 to 510 nm. To estimate lipid peroxidation in vitro, 6 lacs cells per well were seeded in 6-well plates and treated with RSL3 for 6 h or mentioned otherwise. After completion of treatment, cells were incubated with 5 μM BODIPY C11 in the CO_2 incubator for 30 min. After incubation, cells were harvested with TrypLE, washed with DPBS, and analysed by FACS Calibur (BD). Acquired data were analysed using FlowJo software.

4.7. Generation of stable cell lines by lentiviral transduction

3rd generation lentiviral vector pUltra-Chili-Luc (addgene no. 48688) with the bi-cistronic expression of tdTomato and luciferase was used to make HT29 cells fluorescent tagged. Lentiviral particles were generated in HEK-293T cells. Transduction was carried out in the presence of Polybrene (8 μg/ml). A population of transduced cells (HT29-Chili-Luc) was identified by chilli red expression and sorted by flow cytometry. For *PERK, SLC7A11*, and *ATF4* knockdown generation, shRNA sequences were cloned into the 3rd generation transfer plasmid pLKO.1 TRC cloning vector (Addgene cat no. 10878) between unique AgeI and EcoRI sites downstream of the U6 promoter. HEK-293T cell line was used to generate lentiviral particles using the transfection reagent Lipofectamine 3000. The media containing the viral particles was supplemented with Polybrene (8 μg/ml) for transduction. Cells were subjected to puromycin selection after 48 h of transduction, and the knockdown profile of PERK, SLC7A11, and ATF4 was confirmed after 1 week of selection via Western blot. Following oligo sequences were used to clone *PERK, SLC7A11* and *ATF4* shRNA in pLKO.1 plasmid.

shRNA sequence details for *PERK*. *SLC7A11* and *ATF4*.

Gene name	shRNA sequence (5'- 3')
PERK	CCGGGGAACGACCTGAAGCTATAAACTCGAGTTTATAGCT TCAGGTCGTTCCTTTTTG
SLC7A11	CCGGCCTGTCACTATTTGGAGCTTTCTCGAGAAAGCTCCA AATAGTGACAGGTTTTTG
ATF4	CCGGGCCTAGGTCTCTTAGATGATTCTCGAGAATCATCTAAGAGA CCTAGGCTTTTTG

4.8. Generation of stable SLC7A11 overexpression cell lines

The SLC7A11 ORF was amplified from the cDNA of the total RNA of HEK293 cells. The amplified product and pLJM1-EGFP (Plasmid #19319) were further digested with NheI and AgeI restriction enzymes to produce sticky ends on both. After cloning, HEK293T cells were used for viral soup generation. The Viral particles in the presence of Polybrene (8 μg/ml) were added to culture plates containing HT29 EV and PERK KD cells. Transformed cells were cultured for 3 days, and EGFP-positive cells were sorted in BD FACSAria. After culturing the cells for 1-week cells were subjected to Western blot analysis to confirm the expression of SLC7A11. The following primer sets were used to amplify the SLC7A11 ORF from HEK293 cells.

SLC7A11 primer sequence for ORF amplification.

Primer	primer sequence (5'- 3')
Forward	AGAGGCTAGCATGGTCAGAAAGCCTGTTGTGT
Reverse	TATTACCGGTTCATAACTTATCTTCTTCTGGT

4.9. Real-time quantitative PCR (RT-qPCR)

Total RNA was isolated from the cultured cells and tissues using the standard procedure of the RNeasy Mini Kit (Qiagen, cat no.74104). The concentration and purity of the RNA samples were determined using nanodrop. The total RNA (1 μg) of each sample was reverse-transcribed (RT) with random hexamer according to the manufacturer's protocol (Verso cDNA synthesis kit). The final cDNA was diluted with nuclease-free water (1:5), and 10 ng of diluted cDNA was used for each reaction in real-time PCR. Real-time PCR was carried out using an ABI 7500 Real-Time PCR System (Applied Biosystems). Reactions for each sample were performed in triplicate. 18s amplification was used as the housekeeping gene control. The Standard delta-delta Ct method was used to calculate the relative fold change in gene expression. For amplifying *PERK*, *ATF4*, and *SLC7A11*, we performed SYBR Green-based RT-PCR following the manufacturer's (PowerUp SYBR Green ABI) instructions.

4.10. Chromatin immunoprecipitation (ChIP) assay

Following the manufacturer's protocol, ChIP assay was conducted using the CUT&RUN Assay Kit (cat# 86652 Cell Signaling Technology). In brief, cells at 80% confluency were fixed with 1% formaldehyde for 10 min. Cells were then centrifuge washed, followed by lysis in 200 μl of membrane extraction buffer containing protease inhibitor cocktail. The cell lysates were digested with MNase for 30 min at 37°C to get chromatin fragments of 100-500 bp long DNA fragments. Incubation with ATF4 rabbit monoclonal primary antibody, normal IgG, and anti-histone 3 (H3) was done overnight at 4°C. After washing with the wash buffer three times, elution of chromatin from Antibody/Protein A Magnetic beads and reversal of cross-linking was carried out by heat. Spin columns purified DNA then used for SYBR Green-based real-time PCR. The following primers were used to amplify the -328bp site on *SLC7A11* promoter forward primer- 5'CTACTCACAAAACAGTCGCA3', reverse primer- 5'GCAACTCGTAGTGAGCAACAA3', and -494bp and -447bp sites were amplified using forward primer- 5'ATTGGATTTGACTGTATTGCCTT3' and reverse primer-5'CATTGTTTATAACAACACAGTTTGA3'.

4.11. Cloning of SLC7A11 promoter in luciferase reporter vector and luciferase assay

The following primers were used to PCR amplify the *SLC7A11* promoter -0.6 kb upstream of the TSS from the HEK293 cell line-forward primer- 5'TCGGCTAGCGAGGAAGGCTTATAGTTGTGTGTATGTGAC3', reverse primer-5'AGCCTCGAGCAGCTCAGCTTCCTCATGGGC3'. The amplified fragments were cloned into the PGL4.12 [luc2 CP] vector between the NheI and XhoI restriction sites. HT29 cells were seeded in a 6-well plate up to 50–60% confluency and transfected with 2.5 μg of cloned PGL4.12 and 50 ng of PGL4 (hRluc-CMV) plasmid using lipofectamine-3000 as transfection reagent (Invitrogen). The transfected cells with cloned pGL4.12 and pGL4 (hRluc-CMV) were treated with vehicle control or two doses (5 μM and 1 μM) of PERK inhibitor (GSK2656157) or RSL3 (500 nM and 1 μM) for 24 h. Cells were lysed with 100 μL of lysis buffer provided with the Dual-Glo Luciferase assay kit (Promega). The GloMax® 96 Microplate Luminometer was used to measure the activity of Firefly and Renilla luciferases according to the manufacturer's protocol (Promega). For each sample, firefly luciferase activity was normalised to Renilla luciferase activity, and fold change in luciferase activity in different treatment groups was calculated.

4.12. In vivo studies in xenograft tumor models

All animal studies were conducted following standard principles and procedures approved by the Institutional Animal Ethics Committee (IAEC) of CSIR-Central Drug Research Institute. All the animals were maintained in a pathogen-free facility under a day-night cycle. Mice were randomly assigned to groups by a blinded independent investigator. Following our well-established colorectal cancer xenograft models [3], we inoculated 2×10^6 cells (HT29 EV and HT29 PERK KD each) in 100 μl PBS subcutaneously into the flanks of the left or right hind leg of each 4–6 weeks old nude Crl: CD1-Foxn1^{nu} mice. Throughout the study, the tumors were measured with an electronic vernier caliper at regular intervals, and the tumor volumes were calculated using the standard formula V=(W (2) × L)/2, where 'W' is the short and 'L' is the long tumor axis. At the end of the experiment, mice were sacrificed, and subcutaneous tumors were dissected for further studies.

4.13. Immunohistochemistry of tumor tissues

Harvested tumors were fixed in 10% neutral buffered formalin (NBF), and paraffin blocks were prepared for sectioning. For staining, tissue sections were deparaffinised and rehydrated by passing through serial dilutions of xylene and ethanol. Antigen retrieval was performed in 10 mM sodium citrate buffer (pH 6.2) by heating at 95°C for 20–30 min. Processed slides were washed in PBS for 5 min. We used VECTASTAIN ABC KIT (VECTOR laboratories) for IHC staining. ImmEdge pen (hydrophobic barrier pen), and Bloxall blocking solution, were purchased from Vector Laboratories, Inc. Fluorochrome conjugated secondary antibodies, ProLong™ Gold Antifade Mountant, were purchased from molecular Probes-Invitrogen. The endogenous peroxide activity was neutralised by incubating the slides with BLOXALL blocking solution for 10 min. After washing, tissue sections were incubated with diluted normal blocking buffer for 20 min to prevent non-specific staining. The sections were incubated overnight at 4°C with primary antibodies of 4-HNE and MDA diluted in buffer (1:100). The sections were incubated with biotinylated secondary antibody for 1 h, followed by VECTASTAIN ABC Reagent for 30 min. Slides were incubated with diaminobenzidine (DAB) as a chromogen and counterstained with hematoxylin. Negative control sections were processed in parallel without

the primary antibody incubation. The sections were dehydrated and mounted using DPX (Sigma). Stained sections were examined under a microscope (EVOS XL core) under 10x and 40x magnification. ImageJ software was used for scoring 4-HNE and MDA staining. The color deconvolution tool split the IHC images into three color images separately, showing different staining intensities. After adjusting the threshold, images were changed in binary. Analyse the particle tool was used to get the average value of pixels in the DAB channel. ATM score was calculated following the standard formula (Refs) ATM Score = 1/255 (the average value of all the pixels in the DAB channel), where ATM stands for Average Threshold Measure, and 255 is the value of maximum staining intensity [61,62].

4.14. Analysis of TCGA colorectal cancer dataset

Illumina HiSeq mRNA data from GDC TCGA colorectal Cancer (n = 471) was downloaded from the TCGA portal for *PERK* and *SLC7A11* genes using the UCSC Xena browser (https://xena.ucsc.edu) [63]. Log2 (fpkm-uq + 1) values for *PERK* and *SLC7A11* were used to draw a scatter plot. Pearson's correlation coefficient (r) and p-value were calculated in excel.

4.15. Patient samples collection and RNA isolation

Patient samples were scrutinised following the set criteria. A total of 15 CRC tumors with paired normal colorectal mucosa samples were collected from RGCIRC (Rajiv Gandhi Cancer Institute and Research Centre), India, from 2016 to 2019. It was ensured that the tumor was sporadic and the patient had not received chemotherapy or radiotherapy before surgery. The pathologist ensured the total oncogenic area of cancerous cells was not less than 80%. Informed consent was obtained from each patient. The ethical approval of the study was approved by the Institute Ethics Committee, Motilal Nehru National Institute of Technology Allahabad (Ref. No. IEC17-18/027). Total RNA was extracted from tumor tissues using RNeasy Mini Kit (Qiagen, cat no.74104), and RNA concentration and quality were estimated using nanodrop (BioTek Take3). The cDNA preparation and RT-PCR analysis were done as described above.

5. Statistics

In the figure legends, most in vitro experiments represent at least two or more independent experiments or specified otherwise. Student's t-test was used to examine statistically significant differences for two-group analysis. All data are presented as means ± SD or SEM. These analyses were done with Graph-Pad Prism software. Results were considered statistically significant when p values ≤ 0.05 between groups.

Availability of data and materials

All data needed to evaluate the conclusions in the paper are present in the paper and/or in the Supplementary Information. Additional data related to this manuscript will be made available upon reasonable request.

Author contributions

KKS was involved in study designing, performed experiments and wrote the draft manuscript. MPS performed bioinformatic analysis. PC, ABS, MAK AV, MAN, SRS, SM, and AS helped in carrying out in vitro and in vivo studies. SS provided support for patient sample data generation. JS helped in animal maintenance and experimentation. DD conceived the idea, designed experiments, analysed data, wrote the manuscript and provided overall supervision. All authors read and approved the final manuscript.

Declaration of competing interest

The authors declare no conflict of interest related to this manuscript.

Data availability

Data will be made available on request.

Acknowledgments

We sincerely acknowledge the excellent technical help of Mr. A. L. Vishwakarma of SAIF for the Flow Cytometry studies, Mr. Ajay Singh Verma for Luciferase assays. Authors are immensely grateful to Dr. Juhi Tayal, Dr. Anurag Mehta, Dr. DC Doval and Ms. Somika Tiwari (Biorepository, Rajiv Gandhi Cancer Institute and Research Centre, New Delhi, India) for colorectal tumor samples. Research of all the authors' laboratories was supported by CSIR Pan-Cancer Grant (HCP-40) and Fellowship grants from CSIR, DBT, and UGC. D.D. acknowledges grant support from CSIR-FTT (MLP-2025), DST (EMR/2016/006935), DBT (BT/AIR0568/PACE-15/18) and ICMR (2019-1350). The Institutional (CSIR-CDRI) communication number for this article is **10645**.

Appendix A. Supplementary data

Supplementary data to this article can be found online at https://doi.org/10.1016/j.redox.2023.102833.

References

[1] H. Sung, J. Ferlay, R.L. Siegel, M. Laversanne, I. Soerjomataram, A. Jemal, F. Bray, Global cancer statistics 2020: GLOBOCAN estimates of incidence and mortality worldwide for 36 cancers in 185 countries, Ca - Cancer J. Clin. 71 (2021) 209–249, https://doi.org/10.3322/CAAC.21660.

[2] A.K. Singh, R.K. Arya, S. Maheshwari, A. Singh, S. Meena, P. Pandey, O. Dormond, D. Datta, Tumor heterogeneity and cancer stem cell paradigm: updates in concept, controversies and clinical relevance, Int. J. Cancer 136 (2015) 1991, https://doi.org/10.1002/IJC.28804. –2000.

[3] M.A. Nengroo, S. Maheshwari, A. Singh, A. Verma, R.K. Arya, P. Chaturvedi, K. K. Saini, A.K. Singh, A. Sinha, S. Meena, A. Gupta, A. Mishra, J. Sarkar, D. Datta, CXCR4 intracellular protein promotes drug resistance and tumorigenic potential by inversely regulating the expression of Death Receptor 5, Cell Death Dis. 12 (2021), https://doi.org/10.1038/S41419-021-03730-8.

[4] A.K. Singh, A. Verma, A. Singh, R.K. Arya, S. Maheshwari, P. Chaturvedi, M. A. Nengroo, K.K. Saini, A.L. Vishwakarma, K. Singh, J. Sarkar, D. Datta, Salinomycin inhibits epigenetic modulator EZH2 to enhance death receptors in colon cancer stem cells, Epigenetics 16 (2021) 1–18, https://doi.org/10.1080/15592294.2020.1789270.

[5] A. Verma, A. Singh, M.P. Singh, M.A. Nengroo, K.K. Saini, S.R. Satrusal, M.A. Khan, P. Chaturvedi, A. Sinha, S. Meena, A.K. Singh, D. Datta, EZH2-H3K27me3 mediated KRT14 upregulation promotes TNBC peritoneal metastasis, Nat. Commun. 13 (2022), https://doi.org/10.1038/S41467-022-35059-X.

[6] M.J. Hangauer, V.S. Viswanathan, M.J. Ryan, D. Bole, J.K. Eaton, A. Matov, J. Galeas, H.D. Dhruv, M.E. Berens, S.L. Schreiber, F. McCormick, M.T. McManus, Drug-tolerant persister cancer cells are vulnerable to GPX4 inhibition, Nature 551 (2017) 247–250, https://doi.org/10.1038/nature24297, 2017 551:7679.

[7] V.S. Viswanathan, M.J. Ryan, H.D. Dhruv, S. Gill, O.M. Eichhoff, B. Seashore-Ludlow, S.D. Kaffenberger, J.K. Eaton, K. Shimada, A.J. Aguirre, S.R. Viswanathan, S. Chattopadhyay, P. Tamayo, W.S. Yang, M.G. Rees, S. Chen, Z.v. Boskovic, S. Javaid, C. Huang, X. Wu, Y.Y. Tseng, E.M. Roider, D. Gao, J.M. Cleary, B. M. Wolpin, J.P. Mesirov, D.A. Haber, J.A. Engelman, J.S. Boehm, J.D. Kotz, C. S. Hon, Y. Chen, W.C. Hahn, M.P. Levesque, J.G. Doench, M.E. Berens, A.F. Shamji, P.A. Clemons, B.R. Stockwell, S.L. Schreiber, Dependency of a therapy-resistant state of cancer cells on a lipid peroxidase pathway, Nature 547 (2017) 453–457, https://doi.org/10.1038/nature23007.

[8] S.J. Dixon, K.M. Lemberg, M.R. Lamprecht, R. Skouta, E.M. Zaitsev, C.E. Gleason, D.N. Patel, A.J. Bauer, A.M. Cantley, W.S. Yang, B. Morrison, B.R. Stockwell, Ferroptosis: an iron-dependent form of nonapoptotic cell death, Cell 149 (2012) 1060–1072, https://doi.org/10.1016/J.CELL.2012.03.042.

[9] B.R. Stockwell, Ferroptosis turns 10: emerging mechanisms, physiological functions, and therapeutic applications, Cell 185 (2022) 2401–2421, https://doi.org/10.1016/J.CELL.2022.06.003.

[10] J.P. Friedmann Angeli, M. Schneider, B. Proneth, Y.Y. Tyurina, V.A. Tyurin, V. J. Hammond, N. Herbach, M. Aichler, A. Walch, E. Eggenhofer, D. Basavarajappa, O. Rådmark, S. Kobayashi, T. Seibt, H. Beck, F. Neff, I. Esposito, R. Wanke, H. Förster, O. Yefremova, M. Heinrichmeyer, G.W. Bornkamm, E.K. Geissler, S. B. Thomas, B.R. Stockwell, V.B. Odonnell, V.E. Kagan, J.A. Schick, M. Conrad,

Inactivation of the ferroptosis regulator Gpx4 triggers acute renal failure in mice, Nat. Cell Biol. 16 (2014) 1180–1191, https://doi.org/10.1038/ncb3064.
[11] S.J. Dixon, D. Patel, M. Welsch, R. Skouta, E. Lee, M. Hayano, A.G. Thomas, C. Gleason, N. Tatonetti, B.S. Slusher, B.R. Stockwell, Pharmacological inhibition of cystine-glutamate exchange induces endoplasmic reticulum stress and ferroptosis, Elife 2014 (2014), https://doi.org/10.7554/ELIFE.02523.
[12] H. Yuan, X. Li, X. Zhang, R. Kang, D. Tang, Identification of ACSL4 as a biomarker and contributor of ferroptosis, Biochem. Biophys. Res. Commun. 478 (2016) 1338–1343, https://doi.org/10.1016/j.bbrc.2016.08.124.
[13] I. Ingold, C. Berndt, S. Schmitt, S. Doll, G. Poschmann, K. Buday, A. Roveri, X. Peng, F. Porto Freitas, T. Seibt, L. Mehr, M. Aichler, A. Walch, D. Lamp, M. Jastroch, S. Miyamoto, W. Wurst, F. Ursini, E.S.J. Arnér, N. Fradejas-Villar, U. Schweizer, H. Zischka, J.P. Friedmann Angeli, M. Conrad, Selenium utilization by GPX4 is required to prevent hydroperoxide-induced ferroptosis, Cell 172 (2018) 409–422, https://doi.org/10.1016/j.cell.2017.11.048, e21.
[14] W.S. Yang, B.R. Stockwell, Synthetic lethal screening identifies compounds activating iron-dependent, nonapoptotic cell death in oncogenic-RAS-harboring cancer cells, Chem. Biol. 15 (2008) 234–245, https://doi.org/10.1016/J.CHEMBIOL.2008.02.010.
[15] P. Koppula, L. Zhuang, B. Gan, Cystine transporter SLC7A11/xCT in cancer: ferroptosis, nutrient dependency, and cancer therapy, Protein Cell 12 (2021) 599–620, https://doi.org/10.1007/s13238-020-00789-5.
[16] H. fa Yan, T. Zou, Q. zhang Tuo, S. Xu, H. Li, A.A. Belaidi, P. Lei, Ferroptosis: mechanisms and links with diseases, Signal Transduct. Targeted Ther. 6 (2021), https://doi.org/10.1038/S41392-020-00428-9.
[17] Y. Xie, W. Hou, X. Song, Y. Yu, J. Huang, X. Sun, R. Kang, D. Tang, Ferroptosis: process and function, Cell Death Differ. 23 (2016) 369–379, https://doi.org/10.1038/CDD.2015.158.
[18] X. Wu, Y. Li, S. Zhang, X. Zhou, Ferroptosis as a novel therapeutic target for cardiovascular disease, Theranostics 11 (2021) 3052–3059, https://doi.org/10.7150/THNO.54113.
[19] G. Wu, Y.Z. Fang, S. Yang, J.R. Lupton, N.D. Turner, Glutathione metabolism and its implications for health, J. Nutr. 134 (2004) 489–492, https://doi.org/10.1093/JN/134.3.489.
[20] S. Doll, B. Proneth, Y.Y. Tyurina, E. Panzilius, S. Kobayashi, I. Ingold, M. Irmler, J. Beckers, M. Aichler, A. Walch, H. Prokisch, D. Trümbach, G. Mao, F. Qu, H. Bayir, J. Füllekrug, C.H. Scheel, W. Wurst, J.A. Schick, V.E. Kagan, J.P.F. Angeli, M. Conrad, ACSL4 dictates ferroptosis sensitivity by shaping cellular lipid composition, Nat. Chem. Biol. 13 (2017) 91–98, https://doi.org/10.1038/nchembio.2239.
[21] Y.S. Lee, D.H. Lee, H.A. Choudry, D.L. Bartlett, Y.J. Lee, Ferroptosis-induced endoplasmic reticulum stress: cross-talk between ferroptosis and apoptosis, Mol. Cancer Res. 16 (2018) 1073–1076, https://doi.org/10.1158/1541-7786.MCR-18-0055.
[22] D. Ron, P. Walter, Signal integration in the endoplasmic reticulum unfolded protein response, Nat. Rev. Mol. Cell Biol. 8 (2007) 519–529, https://doi.org/10.1038/NRM2199.
[23] S. Wang, R.J. Kaufman, The impact of the unfolded protein response on human disease, J. Cell Biol. 197 (2012) 857–867, https://doi.org/10.1083/JCB.201110131.
[24] P. Walter, D. Ron, The unfolded protein response: from stress pathway to homeostatic regulation, Science 334 (2011) 1081–1086, https://doi.org/10.1126/SCIENCE.1209038.
[25] D. Pincus, M.W. Chevalier, T. Aragón, E. van Anken, S.E. Vidal, H. El-Samad, P. Walter, BiP binding to the ER-stress sensor Ire1 tunes the homeostatic behavior of the unfolded protein response, PLoS Biol. 8 (2010), https://doi.org/10.1371/JOURNAL.PBIO.1000415.
[26] D.T.W. Ng, P. Walter, ER membrane protein complex required for nuclear fusion, JCB (J. Cell Biol.) 132 (1996) 499–509, https://doi.org/10.1083/jcb.132.4.499.
[27] H.P. Harding, Y. Zhang, D. Ron, Protein translation and folding are coupled by an endoplasmic-reticulum-resident kinase, Nature 397 (1999) 271–274, https://doi.org/10.1038/16729.
[28] H. Yoshida, T. Matsui, A. Yamamoto, T. Okada, K. Mori, XBP1 mRNA is induced by ATF6 and spliced by IRE1 in response to ER stress to produce a highly active transcription factor, Cell 107 (2001) 881–891, https://doi.org/10.1016/S0092-8674(01)00611-0.
[29] M. Calfon, H. Zeng, F. Urano, J.H. Till, S.R. Hubbard, H.P. Harding, S.G. Clark, D. Ron, IRE1 couples endoplasmic reticulum load to secretory capacity by processing the XBP-1 mRNA, Nature 415 (2002) 92–96, https://doi.org/10.1038/415092A.
[30] K. Yamamoto, T. Sato, T. Matsui, M. Sato, T. Okada, H. Yoshida, A. Harada, K. Mori, Transcriptional induction of mammalian ER quality control proteins is mediated by single or combined action of ATF6alpha and XBP1, Dev. Cell 13 (2007) 365–376, https://doi.org/10.1016/J.DEVCEL.2007.07.018.
[31] J. Ye, R.B. Rawson, R. Komuro, X. Chen, U.P. Davé, R. Prywes, M.S. Brown, J. L. Goldstein, ER stress induces cleavage of membrane-bound ATF6 by the same proteases that process SREBPs, Mol. Cell. 6 (2000) 1355–1364, https://doi.org/10.1016/S1097-2765(00)00133-7.
[32] C. Hetz, F.R. Papa, The unfolded protein response and cell fate control, Mol. Cell. 69 (2018) 169–181, https://doi.org/10.1016/j.molcel.2017.06.017.
[33] L. Sisinni, M. Pietrafesa, S. Lepore, F. Maddalena, V. Condelli, F. Esposito, M. Landriscina, Endoplasmic reticulum stress and unfolded protein response in breast cancer: the balance between apoptosis and autophagy and its role in drug resistance, Int. J. Mol. Sci. 20 (2019), https://doi.org/10.3390/ijms20040857.
[34] Y.S. Lee, D.H. Lee, H.A. Choudry, D.L. Bartlett, Y.J. Lee, Ferroptosis-induced endoplasmic reticulum stress: cross-talk between ferroptosis and apoptosis, Mol. Cancer Res. 16 (2018) 1073–1076, https://doi.org/10.1158/1541-7786.MCR-18-0055.
[35] A.M. Martinez, A. Kim, W.S. Yang, Detection of ferroptosis by BODIPY™ 581/591 C11, Methods Mol. Biol. 2108 (2020) 125–130, https://doi.org/10.1007/978-1-0716-0247-8_11/COVER.
[36] A. Ayala, M.F. Muñoz, S. Argüelles, Lipid peroxidation: production, metabolism, and signaling mechanisms of malondialdehyde and 4-hydroxy-2-nonenal, Oxid. Med. Cell. Longev. 2014 (2014), https://doi.org/10.1155/2014/360438.
[37] H. fa Yan, T. Zou, Q. zhang Tuo, S. Xu, H. Li, A.A. Belaidi, P. Lei, Ferroptosis: mechanisms and links with diseases, Signal Transduct. Targeted Ther. 6 (2021), https://doi.org/10.1038/s41392-020-00428-9.
[38] Z. Zhang, L. Zhang, L. Zhou, Y. Lei, Y. Zhang, C. Huang, Redox signaling and unfolded protein response coordinate cell fate decisions under ER stress, Redox Biol. 25 (2019), https://doi.org/10.1016/j.redox.2018.11.005.
[39] M. Corazzari, M. Gagliardi, G.M. Fimia, M. Piacentini, Endoplasmic reticulum stress, unfolded protein response, and cancer cell fate, Front. Oncol. 7 (2017) 78, https://doi.org/10.3389/fonc.2017.00078.
[40] C. Hetz, The unfolded protein response: controlling cell fate decisions under ER stress and beyond, Nat. Rev. Mol. Cell Biol. 13 (2012) 89–102, https://doi.org/10.1038/nrm3270.
[41] D. Shin, E.H. Kim, J. Lee, J.L. Roh, Nrf2 inhibition reverses resistance to GPX4 inhibitor-induced ferroptosis in head and neck cancer, Free Radic. Biol. Med. 129 (2018) 454–462, https://doi.org/10.1016/J.FREERADBIOMED.2018.10.426.
[42] K.K. Saini, P. Chaturvedi, A. Verma, M.A. Nengroo, A. Sinha, A.K. Singh, S. Meena, M.A. Khan, M.P. Singh, D. Datta, PERK arm of UPR selectively regulates ferroptosis in colon cancer cells by modulating the expression of system x_c^- (SLC7A11) [abstract], in: Proceedings of the American Association for Cancer Research Annual Meeting 2022; 2022 Apr 8-13, 82, AACR; Cancer Res, Philadelphia (PA), 2022 (12_Suppl):Abstract nr 6249.
[43] Y.H. Shi, Z. bin Ding, J. Zhou, B. Hui, G.M. Shi, A.W. Ke, X.Y. Wang, Z. Dai, Y. F. Peng, C.Y. Gu, S.J. Qiu, J. Fan, Targeting autophagy enhances sorafenib lethality for hepatocellular carcinoma via ER stress-related apoptosis, Autophagy 7 (2011) 1159–1172, https://doi.org/10.4161/AUTO.7.10.16818.
[44] E. Vladykovskaya, S.D. Sithu, P. Haberzettl, N.S. Wickramasinghe, M.L. Merchant, B.G. Hill, J. McCracken, A. Agarwal, S. Dougherty, S.A. Gordon, D.A. Schuschke, O. A. Barski, T. O'Toole, S.E. D'Souza, A. Bhatnagar, S. Srivastava, Lipid peroxidation product 4-hydroxy-trans-2-nonenal causes endothelial activation by inducing endoplasmic reticulum stress, J. Biol. Chem. 287 (2012) 11398–11409, https://doi.org/10.1074/JBC.M111.320416.
[45] M.-H. Lin, J.-H. Yen, C.-Y. Weng, L. Wang, C.-L. Ha, M.-J. Wu, Lipid peroxidation end product 4-hydroxy-trans-2-nonenal triggers unfolded protein response and heme oxygenase-1 expression in PC12 cells: roles of ROS and MAPK pathways, Toxicology 315 (2014) 24–37, https://doi.org/10.1016/j.tox.2013.11.007.
[46] Y. Chen, Y. Mi, X. Zhang, Q. Ma, Y. Song, L. Zhang, D. Wang, J. Xing, B. Hou, H. Li, H. Jin, W. Du, Z. Zou, Dihydroartemisinin-induced unfolded protein response feedback attenuates ferroptosis via PERK/ATF4/HSPA5 pathway in glioma cells, J. Exp. Clin. Cancer Res. 38 (2019) 402, https://doi.org/10.1186/S13046-019-1413-7.
[47] H. Jiang, C. Wang, A. Zhang, Y. Li, J. Li, Z. Li, X. Yang, Y. Hou, ATF4 protects against sorafenib-induced cardiotoxicity by suppressing ferroptosis, Biomed. Pharmacother. 153 (2022), https://doi.org/10.1016/J.BIOPHA.2022.113280.
[48] S.B. Cullinan, J.A. Diehl, PERK-dependent activation of Nrf2 contributes to redox homeostasis and cell survival following endoplasmic reticulum stress, J. Biol. Chem. 279 (2004) 20108–20117, https://doi.org/10.1074/JBC.M314219200.
[49] J.E. Jang, J.I. Eom, H.K. Jeung, H. Chung, Y.R. Kim, J.S. Kim, J.W. Cheong, Y. H. Min, PERK/NRF2 and autophagy form a resistance mechanism against G9a inhibition in leukemia stem cells, J. Exp. Clin. Cancer Res. 39 (2020), https://doi.org/10.1186/S13046-020-01565-3.
[50] X. Zheng, B. Liu, X. Liu, P. Li, P. Zhang, F. Ye, T. Zhao, Y. Kuang, W. Chen, X. Jin, Q. Li, PERK regulates the sensitivity of hepatocellular carcinoma cells to high-LET carbon ions via either apoptosis or ferroptosis, J. Cancer 13 (2022) 669–680, https://doi.org/10.7150/jca.61622.
[51] R. Zhao, Y. Lv, T. Feng, R. Zhang, L. Ge, J. Pan, B. Han, G. Song, L. Wang, ATF6α promotes prostate cancer progression by enhancing PLA2G4A-mediated arachidonic acid metabolism and protecting tumor cells against ferroptosis, Prostate 82 (2022) 617–629, https://doi.org/10.1002/PROS.24308.
[52] Y.X. Feng, E.S. Sokol, C.A. del Vecchio, S. Sanduja, J.H.L. Claessen, T.A. Proia, D. X. Jin, F. Reinhardt, H.L. Ploegh, Q. Wang, P.B. Gupta, Epithelial-to-mesenchymal transition activates PERK-eIF2α and sensitizes cells to endoplasmic reticulum stress, Cancer Discov. 4 (2014) 702–715, https://doi.org/10.1158/2159-8290.CD-13-0945/42426/AM/EPITHELIAL-TO-MESENCHYMAL-TRANSITION-ACTIVATES.
[53] Y. Mou, J. Wang, J. Wu, D. He, C. Zhang, C. Duan, B. Li, Ferroptosis, a new form of cell death: opportunities and challenges in cancer, J. Hematol. Oncol. 12 (2019) 1–16, https://doi.org/10.1186/s13045-019-0720-y.
[54] J.Y. Cao, S.J. Dixon, Mechanisms of ferroptosis, Cell. Mol. Life Sci. 73 (2016) 2195–2209, https://doi.org/10.1007/s00018-016-2194-1.
[55] L. Chen, J. He, J. Zhou, Z. Xiao, N. Ding, Y. Duan, W. Li, L.Q. Sun, EIF2A promotes cell survival during paclitaxel treatment in vitro and in vivo, J. Cell Mol. Med. 23 (2019) 6060–6071, https://doi.org/10.1111/JCMM.14469.
[56] P. Ye, J. Mimura, T. Okada, H. Sato, T. Liu, A. Maruyama, C. Ohyama, K. Itoh, Nrf2- and ATF4-dependent upregulation of xCT modulates the sensitivity of T24 bladder carcinoma cells to proteasome inhibition, Mol. Cell Biol. 34 (2014) 3421, https://doi.org/10.1128/MCB.00221-14.
[57] M.E. Torrence, M.R. Macarthur, A.M. Hosios, A.J. Valvezan, J.M. Asara, J. R. Mitchell, B.D. Manning, The mtorc1-mediated activation of atf4 promotes

protein and glutathione synthesis downstream of growth signals, Elife 10 (2021), https://doi.org/10.7554/eLife.63326.

[58] R. Gao, R.K.R. Kalathur, M. Coto-Llerena, C. Ercan, D. Buechel, S. Shuang, S. Piscuoglio, M.T. Dill, F.D. Camargo, G. Christofori, F. Tang, YAP/TAZ and ATF4 drive resistance to Sorafenib in hepatocellular carcinoma by preventing ferroptosis, EMBO Mol. Med. 13 (2021), https://doi.org/10.15252/EMMM.202114351.

[59] V. Vichai, K. Kirtikara, Sulforhodamine B colorimetric assay for cytotoxicity screening, Nat. Protoc. 1 (2006) 1112–1116, https://doi.org/10.1038/NPROT.2006.179.

[60] S. Maheshwari, S.R. Avula, A. Singh, L.R. Singh, G.R. Palnati, R.K. Arya, S. H. Cheruvu, S. Shahi, T. Sharma, S. Meena, A.K. Singh, R. Kant, M. Riyazuddin, H. K. Bora, M.I. Siddiqi, J.R. Gayen, K.v. Sashidhara, D. Datta, Discovery of a novel small-molecule inhibitor that targets PP2A–β-catenin signaling and restricts tumor growth and metastasis, Mol. Cancer Therapeut. 16 (2017) 1791–1805, https://doi.org/10.1158/1535-7163.MCT-16-0584/86850/AM/DISCOVERY-OF-A-NOVEL-SMALL-MOLECULE-INHIBITOR-THAT.

[61] K. Roy Choudhury, K.J. Yagle, P.E. Swanson, K.A. Krohn, J.G. Rajendran, A robust automated measure of average antibody staining in immunohistochemistry images, J Histochem Cytochem 58 (2010) 95–107, https://doi.org/10.1369/jhc.2009.953554.

[62] S. Ram, P. Vizcarra, P. Whalen, S. Deng, C.L. Painter, A. Jackson-Fisher, S. Pirie-Shepherd, X. Xia, E.L. Powell, Pixelwise H-score, A novel digital image analysis-based metric to quantify membrane biomarker expression from immunohistochemistry images, PLoS One 16 (2021), e0245638, https://doi.org/10.1371/JOURNAL.PONE.0245638.

[63] M.J. Goldman, B. Craft, M. Hastie, K. Repečka, F. McDade, A. Kamath, A. Banerjee, Y. Luo, D. Rogers, A.N. Brooks, J. Zhu, D. Haussler, Visualizing and interpreting cancer genomics data via the Xena platform, Nat. Biotechnol. 38 (2020) 675–678, https://doi.org/10.1038/S41587-020-0546-8.